Should I stay or should I go? Spatio-temporal dynamics of Pseudomonas aeruginosa biofilms in microchannel flows

Massinissa Benbelkacem, Gabriel Ramos, Fatima El Garah, Yara Abidine, Christine Roques, Yohan Davit

Should I stay or should I go? Spatio-temporal dynamics of *Pseudomonas aeruginosa* biofilms in microchannel flows

Massinissa Benbelkacem,[1] Gabriel Ramos,[1,2] Fatima El Garah,[2] Yara Abidine,[1] Christine Roques,[2] and Yohan Davit[1]

[1]*Institut de Mécanique des Fluides (IMFT), Université de Toulouse, CNRS, INPT, UPS, Toulouse, France*

[2]*Laboratoire de Génie Chimique (LGC), Université de Toulouse, CNRS, INPT, UPS, Toulouse, France*

Abstract

Flow plays a particularly important role in the development of bacterial colonies and biofilms: advection efficiently transports nutrients, biocides and molecular signals; flow sensing systems modulate the biological response at the cellular level; and hydrodynamic stresses remodel the biomass and induce detachment. Understanding the coupling mechanisms between biofilms and flow remains an important challenge at the interface between microbiology and mechanics. Here, we study the development of *Pseudomonas aeruginosa* in microchannel flows, from the initial adhesion to the formation of mature biofilms. Combining microfluidics with timelapse microscopy, we find that biofilm development features complex spatio-temporal dynamics. We demonstrate that nutrient limitation is the primary driver for the longitudinal distribution of biomass, while a competition between growth and detachment dominates the temporal dynamics. For a broad range of flow conditions, we show that the system never reaches a true steady-state, even after several days, but instead features large fluctuations that stem from successive cycles of sloughing and growth. We also show that detachment is accurately modeled as two separate components in a differential equation for biomass evolution: a continuous sink term describing smooth detachment and a jump stochastic process that captures catastrophic sloughing events. This behavior in microchannels generalizes previous observations in more complex systems, thus suggesting that oscillations due to competitions between growth and detachment are ubiquitous and play an important role in the development and spreading of biofilms in infections, environmental processes and engineering applications. Our approach further opens the way towards a new quantitative approach to a stochastic characterization of biofilm detachment and the different factors that affect this behavior.

I. INTRODUCTION

Fluid flow and transport phenomena control many aspects of the life of bacteria [1], from the motility of cells [2, 3] to the morphology of biofilm colonies [4], and even ecological interactions within populations [5]. As a testimony to the importance of flow, bacteria have evolved specific strategies adapted to their mechanical environment and the rheology of fluids around them [6]. Bacteria have also evolved mechanisms to detect gradients of nutrients or toxic substances and adapt their movement accordingly [7]. Recent studies further suggest that bacteria have mechanosensing and rheosensing capabilities [6]. For example, *Pseudomonas aeruginosa* has been found to regulate the *fro* operon in response to the shear rate [8]. Shear also modifies the intracellular levels of cyclic-di-GMP in cells of *P. aeruginosa* attached to a surface, initiating a sessile phenotype [3].

Even in dense surface-associated colonies known as biofilms [9, 10], where cells are partially isolated from the fluid by a matrix of self-produced extracellular polymeric substances [11], flow still plays a fundamental role [12, 13]. The flow of a viscous fluid around the matrix generates forces that can induce detachment or remodel the biofilm [14, 15] – the matrix essentially behaves as a viscoelastic material [16] and thus can flow in response to stress [17]. Furthermore, key solutes, such as oxygen or nutrients, are transported in the fluid before they can diffuse in the biofilm and be consumed. This can lead to complex couplings between advective transport by flow, diffusion in the fluid and in the biofilm, and uptake by the cells [18, 19]. It has also been recently demonstrated that flow can generate spatial heterogeneities in the activation of quorum-sensing within populations, as a result of autoinducers being washed away by flow in zones at high Péclet number [20–22].

In many systems, in particular in confined environments [23], a two-way coupling develops between biofilm growth/maturation and transport phenomena: flow and transport mediate the development of the biofilm, but in return the development of the biofilm also modifies flow and transport [24–30]. Perhaps the most dramatic example of this feedback mechanism is bioclogging, as found in pipes or porous media. In such systems, the complex couplings between flow, mass transport and biofilm development can lead to strongly nonlinear responses. For example, biofilm streamers in curvy channels can act as a net that captures planktonic cells and generate extremely fast clogging [31]. In porous media, Kurz *et al.* [32] have showed that a *Bacillus subtilis* biofilm can clog a large part of the pore space, leaving only few preferential flow channels where a competition between shear-induced detachment and growth drives intermittency and spontaneous pressure fluctuations. Even in tubular reactors under constant flow, biofilm development has been shown to result from a competition between cell growth, matrix modification and flow-induced detachment leading to complex dynamics with cycles of pressure rise and drop [33, 34].

Bacteria must resist flow forces in systems ranging from aquifers and riverbeds to the gut

or urinary tract. Bioclogging plays an important role in systems as diverse as bioreactors in the food industry [35], biofilters for wastewater processing [36], pipe flow for water distribution [37], heat exchangers [38] or catheters used in medicine [39]. This clogging can also be used in engineering applications such as soil bioremediation [40], enhanced oil recovery [41, 42] or biobarriers [43]. Understanding the fundamentals of biofilm growth and feedback mechanisms with flow is therefore a crucial step towards developing better approaches in health and engineering.

Here, our goal is to investigate couplings between nutrient transport, growth, remodeling and detachment in microchannel flows. To do so, we developed a microfluidic setup generating a constant flow rate in a microchannel where a *P. aeruginosa* PAO1 GFP biofilm develops. This microfluidic system is further combined with timelapse microscopy, microrheology, cellular microbiology and mathematical modeling to study the interactions between biofilm and flow, in particular the dynamics and spatio-temporal fluctuations.

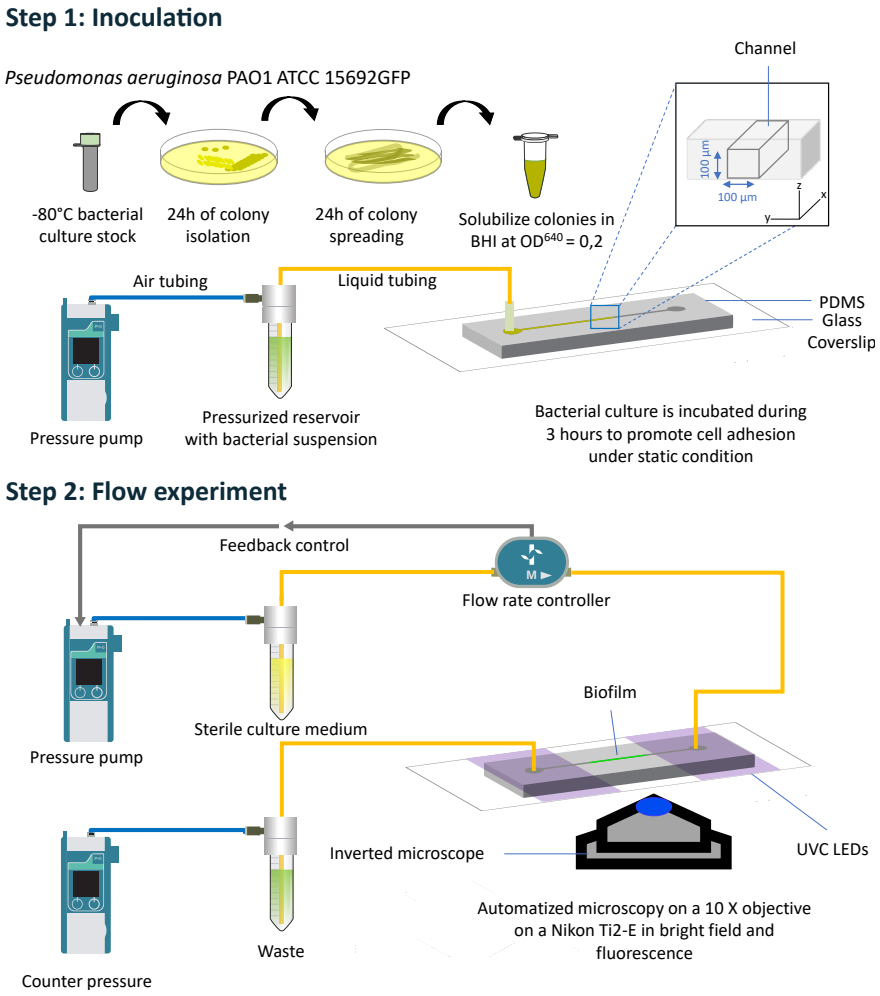

Figure 1: Schematic representation of the system and of the two main experimental steps. The first step is *P. aeruginosa* PAO1 GFP culture and inoculation in the microchannel (PDMS on glass, 100 $\mu m \times 100\ \mu m$ cross-section) using a pressure pump. The bacterial suspension is then left for 3 hours without flow to allow cells to adhere. The second step consists in flowing the culture medium at constant flow rate through the microchannel, while recording pressure fluctuations and imaging biofilm development via photonic microscopy. UVC radiation is used during the second step of the experiment to constrain the biofilm in a specific part of the channel.

II. RESULTS

Our approach is summarized in Fig 1. We proceeded by first inoculating cells of *P. aeruginosa* PAO1 GFP in a microchannel and then flowed a culture medium to observe biofilm development. We used a novel method to limit the growth of the biofilm within a predetermined zone, whereby the biofilm is constrained in a part of the microchannel using UVC irradiation directly through the PDMS of the microfluidic chips. This approach makes it possible to reduce contamination risk and to avoid unwanted progression/growth of *P. aeruginosa* in the inlet and tubing for several days of experiment [44]. We could

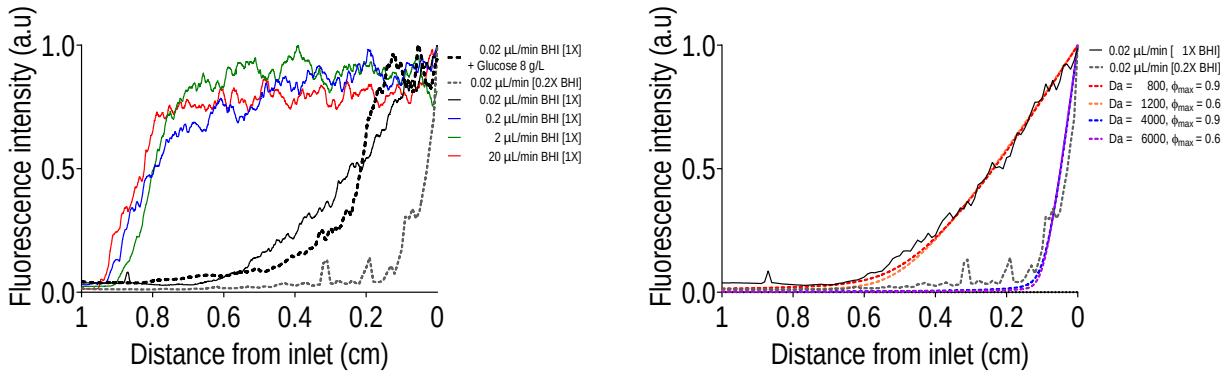

(a) Longitudinal distribution of fluorescence

(b) Simulations for $Q = 0.02\ \mu L/min$

Figure 2: Impact of nutrient limitation on the longitudinal distribution of biofilm. (a): Fluorescence intensity integrated for 72 hours for the flow rates $Q = 0.02\ \mu L/min$, $0.2\ \mu L/min$, $2\ \mu L/min$ and $20\ \mu L/min$ with $1\times$ concentrated brain heart infusion (BHI) culture medium, along with $Q = 0.02\ \mu L/min$ with either $0.2\times$BHI or $1\times$BHI supplemented with $8\ g/L$ glucose. Nutrient limitation is observed only for $Q = 0.02\ \mu L/min$ and is strongly dependent upon the concentration of BHI components. (b): Simulations for $Q = 0.02\ \mu L/min$ for two values of $\phi_{\max}$ and the corresponding Damköhler numbers. The Damköhler numbers for the case with $0.2\times$BHI were simply obtained by multiplying those for the case $1\times$BHI by a factor 5. Each experimental curve in (a) and (b) is averaged over 3 replicates.

thus eliminate parasitic consumption of nutrients in various parts of the fluidic system and maintain a controlled boundary condition with a fixed concentration of nutrients at the inlet of our zone of interest.

In this section, we first use this approach to study the effects of nutrient limitation on the spatial distribution of biofilm in the longitudinal direction. In Section II B, we then detail the temporal evolution to obtain a complete picture of the spatio-temporal dynamics.

A. Couplings between nutrient limitation and flow-induced detachment control the longitudinal distribution of the biofilm

To assess the impact of nutrient limitation on the development of *P. aeruginosa* PAO1 GFP in a microchannel, we performed experiments at different flow rates ($Q = 0.02$, 0.2, 2, and $20\mu L/min$) and therefore different total fluxes of nutrients. Fig 2a (and SI Fig S1) show the time-integrated distributions of the GFP fluorescence in the longitudinal direction for the different flow rates. We found that the active biomass expressing GFP is relatively uniform for all flow rates, except for $0.02\ \mu L/min$. In this case, we observed a maximum value of the fluorescence intensity at the inlet on the right-hand side and a distinct decrease when moving towards the outlet – the sharp decrease on the left-hand side at the outlet corresponds to the effect of the UVCs.

Considering here that the growth of *P. aeruginosa* PAO1 GFP is aerobic – *P. aeruginosa* is a facultative anaerobe and can perform denitrification in anaerobic environments by anoxic respiration using nitrogenated compounds as final electron acceptors [45] but this produces less energy [46] – we hypothesized that this heterogeneity in biofilm development along the channel stems from a limitation of solute species, either oxygen or one (or several) of the nutrients in the growth medium. The idea underlying this hypothesis is that, for the largest flow rates, advective transport through the channel is sufficiently fast compared to consumption, so that even bacteria at the outlet receive sufficient levels of nutrients and oxygen for biofilm development. For the lowest flow rate, however, one of the components introduced at the inlet is rapidly consumed by bacteria and becomes limiting, so that growth decreases with the distance from the inlet.

To better understand this limitation, we proceeded to repeating experiments at 0.02 $\mu L/min$ either with BHI diluted 5 times or by supplementing 1×BHI with additional glucose. Results in Fig 2a with the glucose supplementation show a similar longitudinal distribution of biofilm compared to assays without glucose, thus suggesting that this carbon source is not the limiting nutrient – it was confirmed by mass spectrometry that only a small fraction of the glucose was consumed. Results with the five times diluted BHI, however, show a much narrower window of biofilm growth, therefore suggesting that one or a combination of the components in the BHI is becoming limiting. Although oxygen probably features gradients within the biofilm [47] and in the longitudinal direction, the inlet concentration of oxygen is expected to be identical for the two cases 1×BHI and 0.2×BHI, therefore indicating that oxygen is not the primary component limiting growth. Another factor that may further alleviate oxygen limitations is that PDMS is highly permeable to oxygen, so that there are in fact two sources of oxygen in our system: dissolved oxygen in the culture medium and oxygen transported through the PDMS.

1. A simple conceptualization based on nutrient limitation and logistic growth is insufficient

To further explore these hypotheses and quantify transport characteristic times, we simulated the development of the biofilm inside the channels, taking into account the couplings between biofilm growth and nutrient transport. The limiting nutrient is treated as a solute being transported by advection/diffusion and consumed by bacteria. We considered that mass transport is much faster than bacterial growth and division, so that the problem is quasi-steady for solute transport [19]. The limiting nutrient was thus modeled as

$$\underbrace{Pe\partial_x C^\star}_{\text{Advection}} = \underbrace{\partial_{xx} C^\star}_{\text{Diffusion}} - \underbrace{Da\phi \frac{C^\star}{C^\star + K^\star}}_{\text{Nutrient uptake}}, \tag{1}$$

where $C^\star = \frac{C}{C_0}$ is the non-dimensionalized solute concentration with C $[g \times m^{-3}]$ the con-

Conditions	Variables						
	$\sigma_0\ (Pa)$	$\dot{\gamma}_0\ (s^{-1})$	Pe	$\phi_{\max}$	Da	$\tau_{\text{reac}}\ (s)$	$\frac{Pe}{Da}$
$Q = 0.02\ \mu L/min$ [BHI] = 0.2X	2.4×10^{-3}	2.4×10^{0}	3.3×10^{2}	0.6	6×10^{3}	17	8.3×10^{-2}
				0.9	4×10^{3}	25	5.5×10^{-2}
$Q = 0.02\ \mu L/min$ [BHI] = 1X				0.6	1.2×10^{3}	83	4.2×10^{-1}
				0.9	8×10^{2}	125	2.8×10^{-1}
$Q = 0.2\ \mu L/min$ [BHI] = 1X	2.4×10^{-2}	2.4×10^{1}	3.3×10^{3}	0.989	10^{3}	~ 100	3.3×10^{0}
$Q = 2\ \mu L/min$ [BHI] = 1X	2.4×10^{-1}	2.4×10^{2}	3.3×10^{4}	0.968			3.3×10^{1}
$Q = 20\ \mu L/min$ [BHI] = 1X	2.4×10^{0}	2.4×10^{3}	3.3×10^{5}	0.907			3.3×10^{2}
$Q = 200\ \mu L/min$ [BHI] = 1X	2.4×10^{1}	2.4×10^{4}	3.3×10^{6}	0.786			3.3×10^{3}

Table I: Summary of various quantities in the experiments and models. σ_0 is the shear stress in empty channel. $\dot{\gamma}_0$ is the corresponding shear rate. D is an estimate diffusion coefficient for the limiting component. Pe is the Péclet number. $\phi_{\max}$ is the maximum volumic fraction of biofilm. Da is the Damköhler number. τ_{reac} is the reaction time. $\frac{Pe}{Da}$ is the ratio of Péclet to Damköhler numbers. To calculate dimensionless numbers, we used $D = 10^{-9}\ m^2 s^{-1}$ and $L = 10\ mm$.

centration and $C_0\ [g \times m^{-3}]$ the inlet concentration, x is the longitudinal coordinate system normalized with the length of the channel $L = 10\ mm$, ϕ is the cross-section volume fraction of biofilm and $K\ [g \times m^{-3}]$ the half-saturation constant. Pe is the Péclet number defined as the ratio of longitudinal diffusion to advection times, $Pe = \frac{VL}{D}$ with $V\ [m \times s^{-1}]$ the average velocity in the empty channel and D an estimate diffusion coefficient of the solute – as a reference, for $D = 10^{-9} m^2 \times s^{-1}$, we have $Pe \simeq 330$ for $0.02\ \mu L/min$. Da is the Damköhler number defined as the ratio of diffusive to reactive times, $Da = \frac{\alpha L^2}{C_0 D}$ with $\alpha\ [g \times m^{-3} \times s^{-1}]$ the uptake rate. The term ϕ in the nutrient uptake indicates that consumption is proportional to the volume fraction of biofilm. Reference values are presented in Table I.

For the biomass growth, we first considered a simple model of the form

$$\partial_t \phi = \frac{C^\star\,(1 + K^\star)}{C^\star + K^\star} \phi \left(1 - \frac{\phi}{\phi_{\max}}\right), \tag{2}$$

with time non-dimensionalized with $\frac{X}{Y\alpha(1+K^\star)}$ where $X\ [g \times m^{-3}]$ is the density of the biofilm and Y a yield coefficient – the ratio of biomass created to mass of solute consumed. This

model captures the coupling with consumption via $\frac{C^\star(1+K^\star)}{C^\star+K^\star}$ and the development of the biomass through a logistic growth $\phi\left(1-\frac{\phi}{\phi_{\max}}\right)$ with $\phi_{\max}$ a maximum volume fraction for the biofilm. For the case 0.02 $\mu L/min$, $\phi_{\max}$ corresponds to the maximum volume fraction on the right-hand side of the channel.

There is, however, a major issue with this model. The stable steady-state solution when $C \neq 0$ is $\phi = \phi_{\max}$. Upon resolving this problem numerically, we observed a long-time evolution with a front of biomass slowly progressing towards the outlet, even for very low concentrations of C, until reaching $\phi = \phi_{\max}$ uniformly in the channel.

2. An accurate model requires an explicit description of flow-induced removal

We hypothesized that the problem stems from the logistic growth, which does not accurately capture the flow-induced removal of the biofilm. We thus considered the following model capturing the coupled effects of growth and removal as

$$\partial_t \phi = \underbrace{\frac{C^\star\left(1+K^\star\right)}{C^\star+K^\star}\phi}_{\text{Growth}} - \underbrace{\mathcal{M} f\left(\phi\right)\phi}_{\text{Removal}}, \tag{3}$$

where $f\left(\phi\right) = \sqrt{\frac{\sigma}{\sigma_0}} = \left(1-\phi\right)^{-1}$ with $\sigma = \frac{A}{4}\frac{\mu Q}{h^3}\left(1-\phi\right)^{-2}$ the average tangential stress at the biofilm solid interface (see SI) and $\sigma_0 = \frac{A}{4}\frac{\mu Q}{h^3}$ the shear stress in the empty square cross-section channel (see Table I for reference values). Here A is a scalar parameter characterizing the geometry of the cross-section colonization – $A = \frac{12}{1-\sum_{n,\text{odd}}^{\infty}\frac{1}{n^5}\frac{192}{\pi^5}\tanh\left(n\frac{\pi}{2}\right)} \simeq \frac{12}{1-0.917\times 0.63}$ [48] if we consider a uniform layer of biofilm and only deal with square cross-sections. We also have $\mathcal{M} = \frac{\chi X}{Y\alpha(1+K^\star)}\sqrt{\sigma_0}$, which is the dimensionless number characterizing the competition between growth and detachment, containing the rate of biomass detachment $\chi\ \left[s^{-1}\times N^{-\frac{1}{2}}\times m\right]$. We will consider that $\mathcal{M} \in\ ]0,1]$, which is discussed in what follows.

A number of models in the literature express the detachment rate as proportional to the square root of the fluid shear stress at the biofilm fluid interface Coyte *et al.* [49]. Here this could be written as $f\left(\phi\right) = \sqrt{\frac{\tau_{\text{shear}}}{\sigma_0}} = \left(1-\phi\right)^{-3/4}$ with τ_{shear} the shear stress at the biofilm fluid interface. Such approaches, however, were initially developed for flows in reactor systems where shear stress is dominant [50, 51] and neglect the contribution of the pressure stress to detachment. Characklis *et al.* [52], for instance, measured the rate of biofilm loss under different shear stresses generated by rotating the inner annulus of reactor at different speeds and found a linear relationship between biofilm loss rate and rotational speed. Upon clogging the microchannel, we expect the pressure difference to generate a significant force on the biofilm and to play an important role on detachment. We could have introduced a multi-modal form of detachment, with contributions from both the shear stress at the biofilm/fluid interface, scaling as $\left(1-\phi\right)^{-3/4}$, and the tangential component of the total stress at the biofilm/solid interface, scaling as $\left(1-\phi\right)^{-1}$. For simplicity, however,

we consider a contribution scaling as $(1-\phi)^{-1}$. The model thus reads

$$\partial_t \phi = \frac{C^\star (1+K^\star)}{C^\star + K^\star}\phi - \mathcal{M}\frac{\phi}{1-\phi}. \tag{4}$$

The only non-trivial steady-state of this model is

$$\phi_{\text{equ}} = 1 - \mathcal{M}\frac{C^\star + K^\star}{C^\star (1+K^\star)} \tag{5}$$

and reflects an equilibrium between the amount of biomass created and the amount of biomass detached. When $C^\star$ is lower than $\frac{\mathcal{M}K^\star}{1+K^\star-\mathcal{M}}$, then $\phi_{\text{equ}} = 0$ – more precisely, $\phi_{\text{equ}} = 0$ becomes stable when $C^\star$ is lower than $\frac{\mathcal{M}K^\star}{1+K^\star-\mathcal{M}}$. The maximum value of ϕ_{equ}, which we term $\phi_{\max}$, is obtained when $C^\star = 1$, so that we can express $\mathcal{M}$ as

$$\mathcal{M} = 1 - \phi_{\max} = \frac{\chi X}{Y\alpha (1+K^\star)}\left(\frac{A}{4}\frac{\mu Q}{h^3}\right)^{\frac{1}{2}} \tag{6}$$

and we can write the model as

$$\partial_t \phi = \phi\left[\frac{C^\star (1+K^\star)}{C^\star + K^\star} - \frac{1-\phi_{\max}}{1-\phi}\right], \tag{7}$$

with $\phi_{\max} \in [0,1[$ and $\phi \in [0, \phi_{\max}]$. To parameterize the model, we therefore only need to evaluate the maximum value of the volume fraction for each case, which can be extracted from our experiments in different ways. We also see that, in assuming that $\mathcal{M} \in]0,1]$ and eliminating cases where $\mathcal{M} > 1$, we have not considered situations of systematic detachment $\phi_{\text{equ}} = 0$ for any value of the concentration, since this is not a situation that we encountered experimentally. Also note that we consider only $\phi_{\max} < 1$ to avoid issues with the limit $\lim_{\phi,\phi_{\max}\to 1^-} f$.

This model has two important differences with Eq 2. First, the reaction rate, and thus the solute concentration, is now involved only in the positive part of the rate of change of ϕ, as we assume that it modulates the growth rate and not detachment. This implies that the equilibrium volume fraction depends on the concentration of nutrients and eliminates the previously mentioned problem of the slow evolution of the volume fraction towards a uniform state. The second important difference is that the negative part is now a nonlinear function of ϕ, featuring a dramatic increase of the removal rate as $\phi \to \phi_{\max}$.

Fig 2 compares results of the model with those of the experimental fluorescence for the flow rate 0.02 $\mu L/min$ and $K^\star = 0.1$. We considered that the fluorescence signal is proportional to the product of biomass and concentration. We then integrated this signal in time and normalized it with the maximum value as $\overline{F}(x) = \frac{\int_0^t \phi(x,\tau)C(x,\tau)d\tau}{\int_0^t \phi(x=0,\tau)C(x=0,\tau)d\tau}$. To roughly assess the sensitivity of our simulation to uncertainties in the value of $\phi_{\max}$, we

further considered two extreme values, $\phi_{\max} \simeq 0.6$ and $\phi_{\max} \simeq 0.9$. The model shows good agreement with experiments for $Da_{\mathrm{BHI}\times 1} \simeq 1200$ in the case $\phi_{\max} \simeq 0.6$ and $Da_{\mathrm{BHI}\times 1} \simeq 800$ in the case $\phi_{\max} \simeq 0.9$. The corresponding characteristic reaction time for nutrient uptake is $\tau_{\mathrm{reac}} = \frac{C_0}{\alpha} = \frac{L^2}{D \times Da}$, therefore ranging from $\simeq 83s$ to $\simeq 125s$. We also obtain an excellent correspondence between the model and the experimental data for the 5 times dilution of the BHI without any fitting, simply by multiplying the Damköhler number by a factor 5 – recall that, by definition, $Da = \frac{\alpha L^2}{C_0 D}$ with C_0 the inlet concentration so that dividing C_0 by 5 implies multiplying the Damköhler number by a factor 5. This further confirms that the primary limitation is indeed one or a combination of the components of the BHI, not oxygen.

With the previous estimations of characteristic times for uptake, we can also evaluate whether any form of radial limitation of nutrient is expected. The characteristic time for diffusion in the radial direction is $\tau_{\mathrm{diff}} = \frac{h^2}{D}$ with $h \simeq 50\ \mu m$ a characteristic length for the distance between the flow channel and the wall. Considering again a diffusion coefficient in the biofilm $D = 10^{-9} m^2/s$ for the limiting nutrient – and keeping in mind that we are performing an analysis in orders of magnitude – we have $\tau^h_{\mathrm{diff}} \simeq 2.5\ s$ and the transverse Damköhler number is much lower than one. A gradient of concentration will develop in the radial direction, but only a weak one not generating strong limitations – as a reference, the longitudinal limitation happens here only for the flow rate 0.02 when $\tau^L_{\mathrm{advection}} = \frac{L}{V} \simeq 300s$ and is not present for 0.2 when $\tau^L_{\mathrm{advection}} \simeq 30s$.

For solute transport, the complete picture is therefore that of growth limited by one or a combination of the components of the BHI with:

- in the transverse direction, a weak gradient due to a competition diffusion and reaction, but no strong limitation.

- in the longitudinal direction, a strong limitation only for the flow rate 0.02 $\mu L/min$ due to a competition between advective transport and reaction. When ${}^{Pe}/_{Da} < 1$, reaction occurs faster than transport along the channel so that we are in a nutrient-limited regime. When ${}^{Pe}/_{Da} > 1$, advection is fast enough to provide nutrients throughout the entire channel.

For the biomass, development results from an equilibrium between growth and flow-induced removal. To elucidate further the role of detachment, we now focus on the flow rates $Q =$ 0.2, 2 and 20 $\mu L/min$ that feature no strong nutrient limitation. We study the spatio-temporal dynamics and analyze in detail the nature of detachment.

B. The temporal dynamics reflects a competition between growth and detachment

Here, we describe the temporal dynamics of the process through two classes of measurements. First, we monitored the evolution of the pressure in the inlet reservoir, while imposing a constant flow rate. From this measurement, we could reconstruct the evolution in time of the hydraulic resistance of the zone of interest in the channel, $\mathcal{R}(t)$, where biofilm develops (see Material and Methods). We then plotted the ratio $\frac{\mathcal{R}}{\mathcal{R}_0}$, with $\mathcal{R}_0$ the hydraulic resistance of the empty channel, as shown in Fig 3 (see also supplementary information figures S5, S8 and S11) and used this to analyze the different stages in the colonization of the channel. Combined with a model for the distribution of biofilm in the cross-section of the channel – as before, we assumed that the biofilm is a uniform layer – it was used to indirectly evaluate a mean volume fraction of biofilm, ϕ. Second, we also visualized directly the channel using timelapse microscopy with differential interference contrast, bright field and fluorescence imaging.

Fig 3 shows that there are several stages in the development of the biofilm, similar for the different flow rates, which we have divided into two main components: stage I that corresponds to the initial adhesion, growth and saturation; and stage II that features large fluctuations.

1. Early stage I is driven by surface adhesion, motility, division and microcolony formation

Our inoculation process results in the sparse attachment of individual bacterial cells on the boundaries of the channel. On the glass slide, we evaluated the initial density on the surface to be about 38800 cells per mm^2. Besides attachment, we also observed flow-induced detachment and surface motility, with cells either standing upright [53] or lying on the side. Growth of adhered cells started straight away upon flowing the culture medium. The apparent macroscopic lag, as visible in Fig 3, does not stem from a lag at the cellular level, but rather from the sensitivity of the pressure measurements and from the nonlinear dynamics of clogging. Consider, for instance, a uniform layer of biofilm with a flow channel in the center that has a square cross-section. The relative hydraulic resistance reads $\frac{\mathcal{R}}{\mathcal{R}_0} = \frac{1}{(1-\phi)^2}$, which can be linearized as $\frac{\mathcal{R}}{\mathcal{R}_0} \sim 1+2\phi$ when $\phi \ll 1$. The evolution of $\frac{\mathcal{R}}{\mathcal{R}_0}$ with ϕ is thus affine at the beginning of the experiment, with small changes in the hydraulic conductivity that could not be detected in our experimental system. Colonies then expand and produce large quantities of EPS, resulting in a much sharper increase of the hydraulic resistance. This increase reflects a combination between the exponential growth of the microorganisms, the production of the EPS and the nonlinear relationship between $\frac{\mathcal{R}}{\mathcal{R}_0}$ and ϕ.

To characterize the growth time at the cellular level, we proceeded to the calculation of an apparent doubling time at the cellular level from microscopy images of cells attached to the glass slide in the very early stage (from 0 to 3.5 hours). We first segmented images from differential interference contrast microscopy to identify individual bacteria on the surface

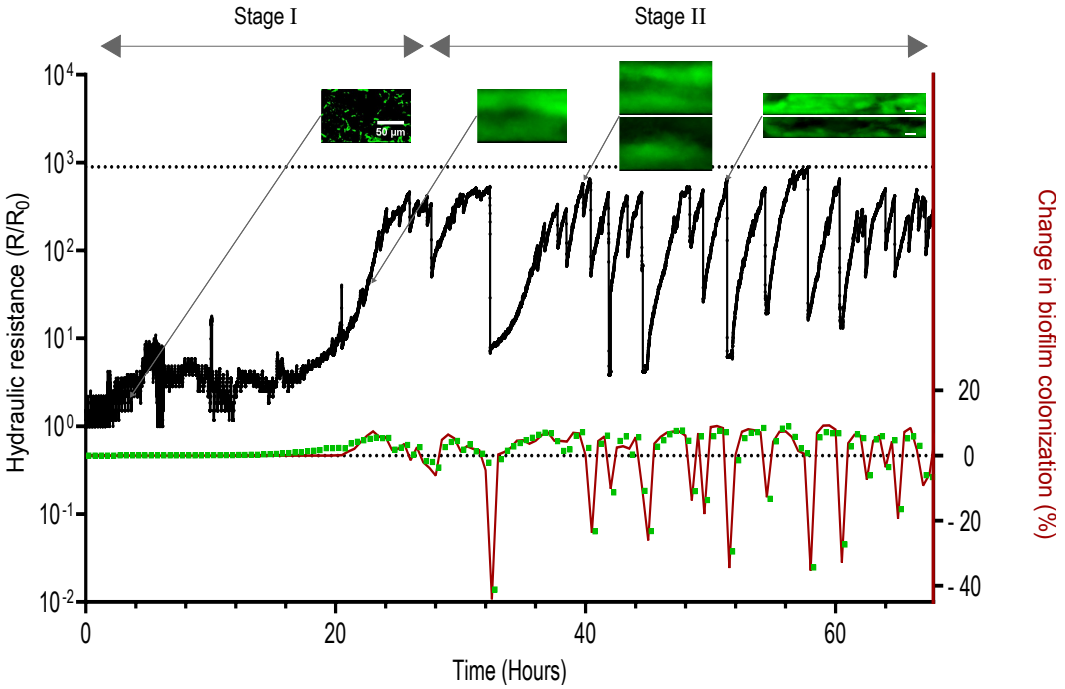

(a) Illustration of growth stages for one experiment at $Q = 0.2\ \mu L/min$

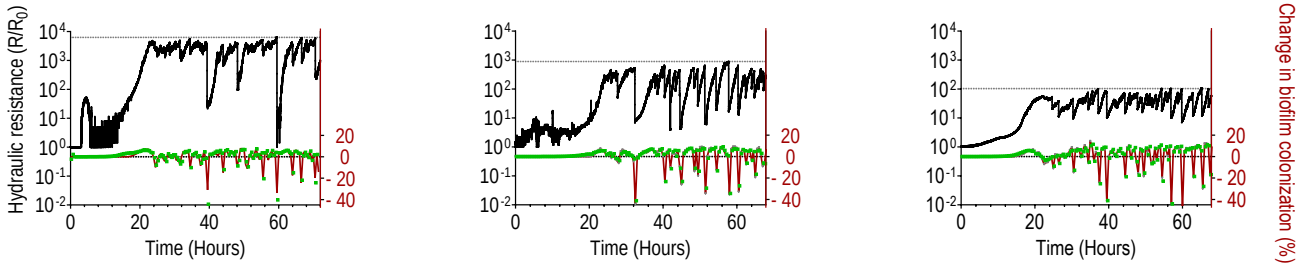

(b) $Q = 0.2\ \mu L/min$ (c) $Q = 2\ \mu L/min$ (d) $Q = 20\ \mu L/min$

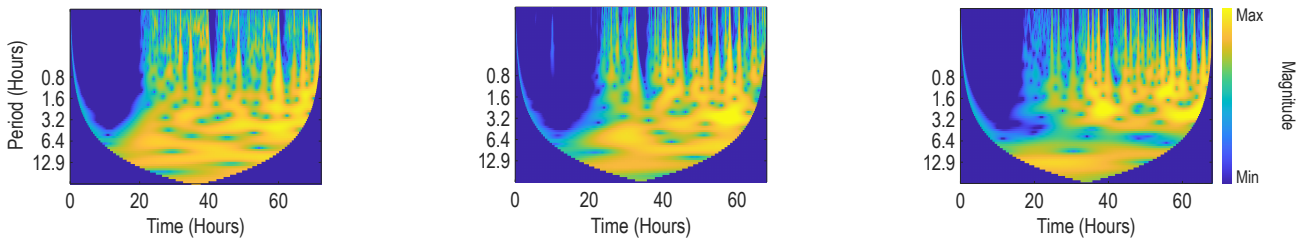

(e) $Q = 0.2\ \mu L/min$ (f) $Q = 2\ \mu L/min$ (g) $Q = 20\ \mu L/min$

Figure 3: Temporal dynamics of growth and detachment for $Q = 0.2\ \mu L/min$, $2\ \mu L/min$ and $20\ \mu L/min$. (a): Summary of the two main stages of biofilm development. The figure shows the evolution of the hydraulic resistance (black solid line) in time, calculated from pressure measurements, and microscopy images corresponding to the different phases. It also shows changes in biofilm colonization extracted from either integrated fluorescence intensity (green squares) or from image segmentation (red solid line). (b), (c) and (d): Temporal dynamics of growth and detachment for the different flow rates. (e), (f) and (g): Wavelet scalograms corresponding to (b), (c) and (d).

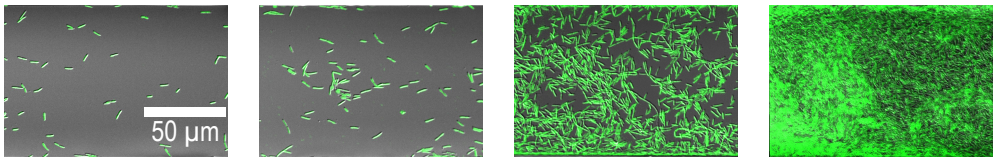

(a) Attached cells 0 h (b) Early microcolony 4 h (c) Microcolony 8 h (d) Biofilm 16 h

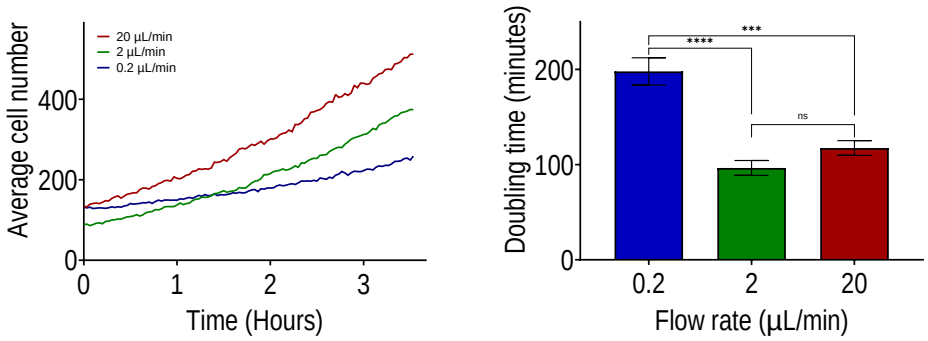

(e) (f)

Figure 4: Flow modifies the apparent doubling time of bacteria on surfaces. (a), (b), (c) and (d): Composite brightfield and GFP images of development stages, starting from single cells that form microcolonies and then evolve towards a biofilm. (e) and (f) show, respectively, the average number of cells on the surface as a function of time and the corresponding doubling time for flow rates ($Q = 0.2\ \mu L/min$, $2\ \mu L/min$ and $20\ \mu L/min$). For (f), statistical differences were examined by unpaired student test with Gaussian distribution of data and equal standard deviations. Error bars indicate standard error of mean (SEM) and symbols denote statistical significance (****:p-value <0.0001, ***: p-value $= 0.0002$, ns: p-value > 0.05). The doubling time was calculated by a linear fitting of the logarithm of the number of cells. The slope was used to estimate growth rate and doubling time. Cell count was calculated from image segmentation of four positions in two channels to generate 8 measurements by condition (n$= 8$) for ($Q = 0.2\ \mu L/min$, $2\ \mu L/min$ and $20\ \mu L/min$).

and then fitted linearly the log of the number of cells as a function of time. Calculated doubling times were measured as about 198, 95 and 117 minutes in average for, respectively, $Q = 0.2\ \mu L/min$, $2\ \mu L/min$ and $20\ \mu L/min$. As a reference, the doubling time in liquid culture was measured as about 110 minutes (standard deviation of ~ 10 minutes). Although understanding exactly what generates this dependence of the doubling time upon the flow rate is beyond the scope of this paper, it is worth noting that:

- nutrient limitation is not likely to play a role, as we have previously validated the fact that there is no limitation for $Q \geq 0.2\ \mu L/min$, even when biofilm has formed.

- mechano- and rheo-sensing could be involved, with bacteria directly regulating their

response to perceived shear stress or rate [3, 8].

- biomass removal plays a role in the dynamics even in this very early stage. For example, considering the previous model in the absence of nutrient limitation, in the limit $\phi \ll 1$ and with an explicit characteristic time for growth, τ, we have $\tau\dot{\phi} = \phi_{\max}\phi$, the solution of which is simply $\phi = \phi\,(t=0)\, e^{\phi_{\max}\frac{t}{\tau}}$. The apparent characteristic time in the exponential growth is therefore $\frac{\tau}{\phi_{\max}}$ (with doubling time $\ln(2)\,\frac{\tau}{\phi_{\max}}$), which provides a time slightly larger than τ accounting for both growth and the detachment at the early stages of attachment.

- heterogeneities in the rate of division could also be important. For example, our visualizations suggest that the proportion of adhered and motile cells could be a function of the flow rate, with a proportion of motile cells that seemed larger at the lowest flow rates (see SI movie S1, S2 and S3). This difference could have an impact on division time with adhered/motile cells exhibiting different growth rates. It has been previously shown by [54] for *Caulobacter crescentus* that the probability of attachment scales with the inverse of an effective Péclet number – this Péclet number compares timsecales for advective transport by the flow and Brownian-like trajectories due to motility – and that the colonization rate of the surface decreases with the flow rate because of the specific way the daughter cell is released in the flow upon division.

2. Late stage I reflects an equilibrium between growth and detachment

Late stage I corresponds to the end of the rapid growth phase, with a removal rate of the biofilm that progressively increases, until it smoothly equilibrates with growth. Considering the balance of biomass in the zone of interest in the channel, the inlet flux of bacteria is zero, since our UVC system prevents growth outside the zone of interest. The source of biomass therefore only results from the uptake of nutrients, division of bacterial cells and EPS production. Flow-induced removal includes parts of the biofilm that are displaced out of the zone of interest through the flow/remodelling of the biofilm at the outlet, and parts that are washed away by erosion and seeding [1, 55]. In the absence of nutrient limitation, we can estimate the evolution of the biovolume in the channel from the ordinary differential equation

$$\dot{\phi} = \phi\left(1 - \frac{1-\phi_{\max}}{1-\phi}\right), \tag{8}$$

which is a direct simplification of Eq 7 with ϕ describing an average volume fraction in the entire channel, and thus being only a function of time. This model can be understood as describing a form of limit behavior that captures different types of smooth detachment (flow,

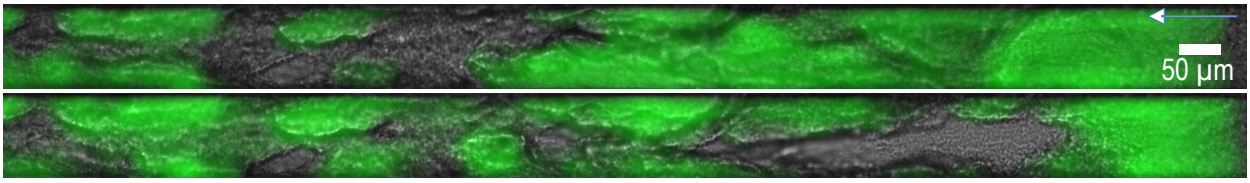

(a) Minor event

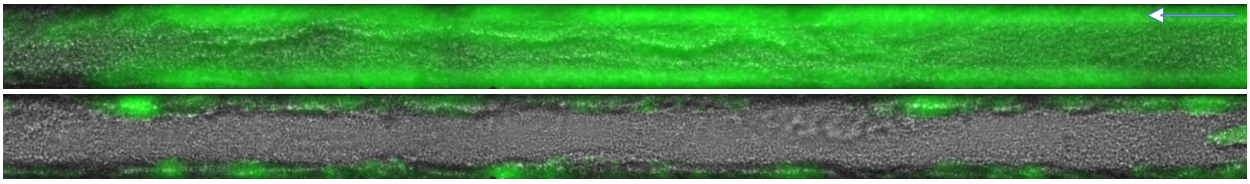

(b) Major event

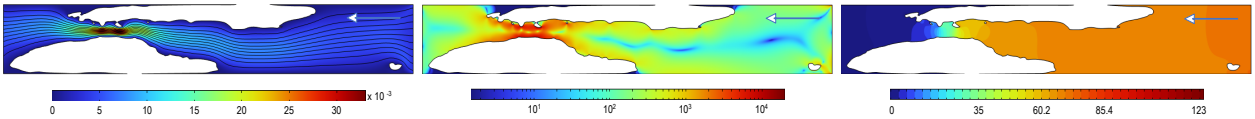

(c) Velocity (m/s) (d) Shear (s^{-1}) (e) Pressure (Pa)

Figure 5: Stage II features sloughing events. (a): Composite brightfield and GFP image of a 40 hour biofilm during stage II. Top and bottom images show biofilm before and after a minor detachment event. (b): Same as (a) for a major detachment event. (c), (d) and (e): 2D simulations of flow around a biofilm (white) in a channel of 100 μm width and 500 μm length using COMSOL multiphysics. (c): Streamlines and magnitude of the velocity (m/s). (d): Shear rate in (s^{-1}). (e): Pressure field in (Pa). The white arrows indicate the flow direction.

seeding, erosion) but not discrete sloughing events that become prominent in Stage II (see Section II B 3).

3. Stage II features sloughing-induced jump events

After growth and detachment start to equilibrate at the end of stage I, sloughing events become particularly important. These are visible in Fig 3 as jumps in the hydraulic resistance (see also the blue stripes on the wavelet scalograms in Fig 3), which correlate with sharp changes in the biofilm colonization of the channel. The jumps correspond to a range of different events, ranging from minor detachment – where a relatively small portion of the biomass is detached – to major sloughing – where a large portion of the biomass is detached. Fig 5 shows example microscopy images of such events. Fig 5 also shows simple 2D flow simulations illustrating the types of stress induced by the flow of a viscous fluid upon the biofilm. We see that the shear stress becomes particularly strong in the bottlenecks and that the pressure difference also builds up, therefore generating both shear and pressure stresses.

A simple approach to quantifying the relative importance of stresses in our system is to consider the case of uniform film growth between the UVC zones (see details in supplemen-

tary information). The tangential stress at the solid/biofilm surface is $\frac{\sigma}{\sigma_0} = (1-\phi)^{-2}$, with a contribution from shear $\frac{\sigma_{\text{shear}}}{\sigma_0} = (1-\phi)^{-1}$ and from pressure $\frac{\sigma_{\text{pressure}}}{\sigma_0} = \phi\,(1-\phi)^{-2}$. In the case of a fixed flow rate, we therefore have $\frac{\sigma_{\text{shear}}}{\sigma_0} \to 1$ and $\frac{\sigma_{\text{pressure}}}{\sigma_0} \to 0$ in the limit $\phi \to 0$; $\sigma_{\text{shear}} = \sigma_{\text{pressure}}$ for $\phi = 0.5$; and $\sigma_{\text{pressure}} > \sigma_{\text{shear}}$ for $\phi > 0.5$. The analysis can also be extended to the case of an applied pressure difference, rather than an imposed flow rate, by expressing stresses as $\frac{\sigma_{\text{shear}}}{4h\Delta P/L} = (1-\phi)^{1/2}$ and $\frac{\sigma_{\text{pressure}}}{4h\Delta P/L} = \phi$. $\frac{\sigma_{\text{shear}}}{4h\Delta P/L}$ then starts at one when $\phi = 0$ and decreases to zero when $\phi = 1$ – complete clogging is possible in the case of an imposed pressure difference – while $\frac{\sigma_{\text{pressure}}}{4h\Delta P/L}$ starts at zero and increases to one, with both curves meeting at $\phi = \frac{\sqrt{5}-1}{2}$. This simple conceptualization confirms that pressure stress tends to become dominant when a large portion of the channel is colonized.

To better visualize the spatio-temporal dynamics and connect the different observations for the pressure and microscopy, we plotted kymographs in Fig 6 (see also SI figures S7, S10 and S13), showing both variations in time and in space, along with the corresponding hydraulic resistance signal. These graphics show clearly the correlation between the pressure signal on the right-hand side and the detachment events on the kymographs. In particular, we can readily identify that large drops in pressure correspond to large events with detachment over almost the entire length of the micro-channel. We also visualize a range of detachment events corresponding to various sizes of biofilm being detached.

4. A critical value of the hydrodynamic stress equilibrates growth and smooth detachment

After each jump event, the volume fraction increases until it reaches again a form of equilibrium or until another jump event occurs. The maximum value of the hydraulic resistance depends on the flow rate and decreases by orders of magnitudes from 0.2 to 20 $\mu L/min$ – $\frac{\mathcal{R}_{\max}}{\mathcal{R}_0} \simeq 8.2 \times 10^3$ for 0.2, $\simeq 8.4 \times 10^2$ for 2 and $\simeq 1.0 \times 10^2$ for 20. The corresponding estimation for the maximum values of the volume fraction are $\phi_{\max}(Q = 0.2) = 0.989$ for 0.2, $\phi_{\max}(Q = 2) = 0.966$ for 2 and $\phi_{\max}(Q = 20) = 0.901$ for 20 (see Fig 7 and Table I). One of the remarkable features of this maximum value is that it is very reproducible across replicates, with standard deviations for volume fractions in the range of 10^{-3} in our experiments (Fig 7). Another remarkable property is that the product $\frac{Q}{Q_{\text{ref}}} \times \frac{\mathcal{R}_{\max}}{\mathcal{R}_0}$ seems approximately constant across flow rates. Since this product is directly proportional to the pressure difference and therefore the stress at the solid interface, we hypothesized that there exists a critical value of the stress, or equivalently a critical value of the volume fraction, for which growth equilibrates with detachment – through biofilm "flow" at the outlet and erosion and seeding in the microchannel.

The model presented so far, in Eq 8, cannot reproduce jump events – we will see in Section II B 5 how the model can be refined to do so. However, it is consistent with the idea of a critical stress that removes enough biomass to equilibrate growth. Our conceptu-

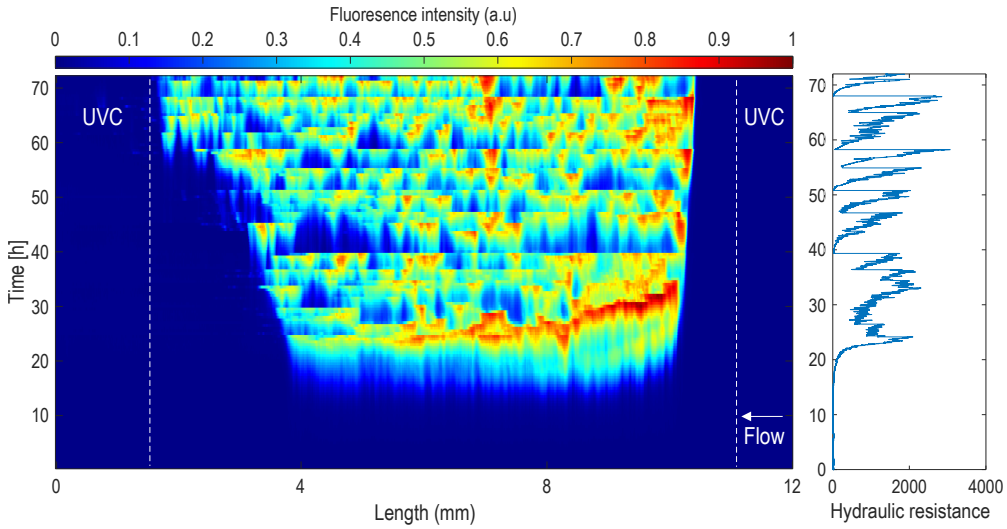

(a) $Q = 0.2\ \mu L/min$

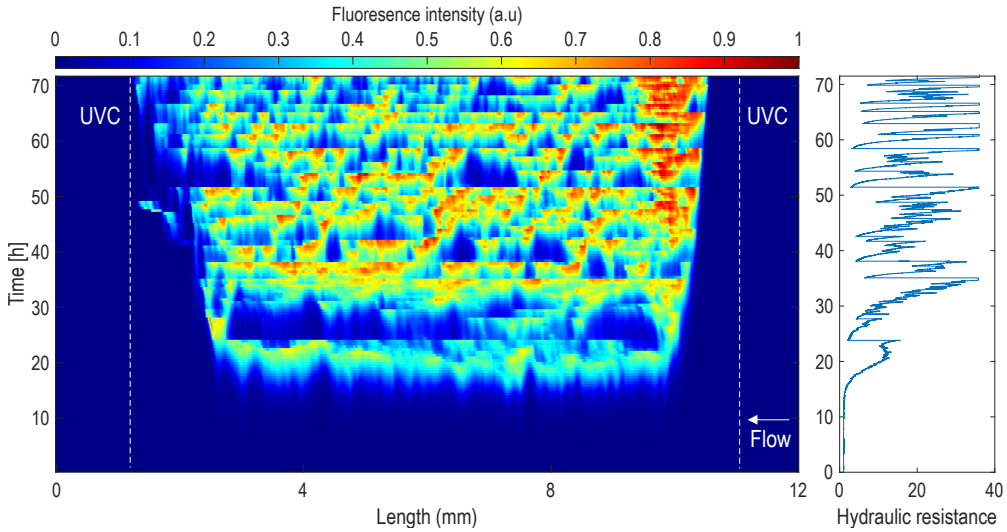

(b) $Q = 20\ \mu L/min$

Figure 6: Spatio-temporal dynamics of biofilm development. Kymographs show the fluorescence intensity (averaged in the radial direction y) as a function of both the longitudinal direction (x) and time. Fluorescence intensity values were normalized by the maximum value. Plots on the right-hand side show the corresponding hydraulic resistance as a function of time.

alization for the steady-state solution is indeed an equilibrium between a constant growth rate and a removal rate that is proportional to the square root of the tangential stress at the biofilm/solid interface. When nutrients are in excess, this model (see Eq 3) captures a critical value of the stress that equilibrates growth as $(1-\phi_{\max})\sqrt{\frac{\sigma_{\text{crit}}}{\sigma_0}} = 1$, which can be written as $\sigma_{\text{crit}} = \frac{\sigma_0}{(1-\phi_{\max})^2} = \sigma_0 \frac{\mathcal{R}_{\max}}{\mathcal{R}_0}$. Given the values of σ_0 (Table I) and the fact that $\frac{\mathcal{R}_{\max}}{\mathcal{R}_0} \simeq 8.2 \times 10^3$ for $0.2\ \mu L/min$, $\simeq 8.4 \times 10^2$ for $2\ \mu L/min$ and $\simeq 1.0 \times 10^2$ for $20\ \mu L/min$, we can estimate this critical stress at roughly $100 - 200\, Pa$.

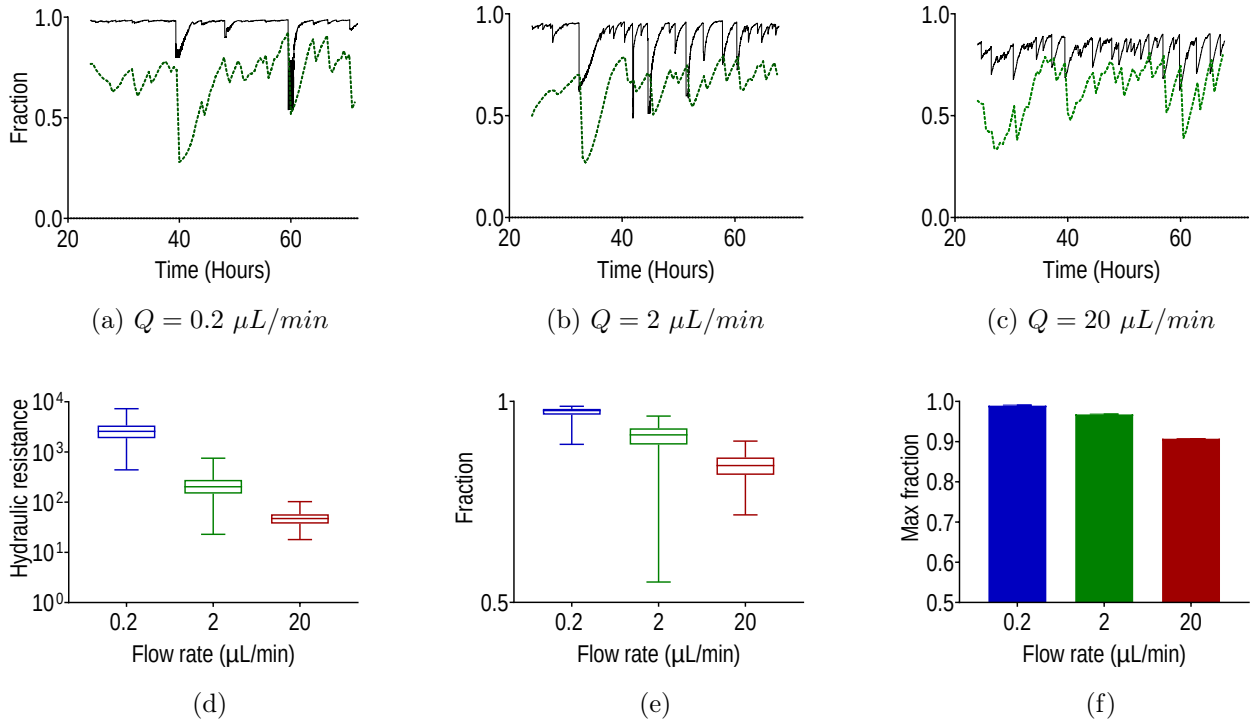

(a) $Q = 0.2\ \mu L/min$ (b) $Q = 2\ \mu L/min$ (c) $Q = 20\ \mu L/min$

(d) (e) (f)

Figure 7: Evolution of the volume fraction for the different flow rates. (a), (b) and (c): Fractions of biofilm in the microchannel, either calculated from hydraulic resistance (black solid line) or estimated from integrated GFP intensity (green dotted line), for the different flow rates. (d) and (e): Distributions of hydraulic resistance and the corresponding biofilm fraction between 24 and 72 h for all flow rates, represented as whisker boxes. (f): Maximal values of biofilm fraction for different flow rates. Error bars represent standard deviation of average values for n = 3.

In the case of an imposed flow rate, we can write that equivalently as a maximum value for the volume fraction of biofilm, $\phi_{\max}$, that reads $\phi_{\max} = 1 - \frac{\chi X}{Y\alpha(1+K^\star)}\left(\frac{A}{4}\frac{\mu Q}{h^3}\right)^{\frac{1}{2}}$. Writing the characteristic reaction time as $\tau_{\text{reac}} = \frac{X}{Y\alpha(1+K^\star)}$, we can also express this relatively to a reference flow rate as

$$\frac{1-\phi_{\max}(Q)}{1-\phi_{\max}(Q_{\text{ref}})} = \frac{\chi(Q)}{\chi(Q_{\text{ref}})}\frac{\tau_{\text{reac}}(Q)}{\tau_{\text{reac}}(Q_{\text{ref}})}\left(\frac{Q}{Q_{\text{ref}}}\right)^{\frac{1}{2}}. \tag{9}$$

Upon assuming that $\frac{\chi(Q)}{\chi(Q_{\text{ref}})}\frac{\tau_{\text{reac}}(Q)}{\tau_{\text{reac}}(Q_{\text{ref}})}$ does not depend on the flow rate, so that $\frac{\chi(Q)}{\chi(Q_{\text{ref}})}\frac{\tau_{\text{reac}}(Q)}{\tau_{\text{reac}}(Q_{\text{ref}})} \simeq 1$, and considering $Q_{\text{ref}} \equiv 0.2$ with $\phi_{\max}(Q_{\text{ref}}) = 0.989$, we obtain $\phi_{\max}^{\text{theoretical}}(Q=2) \simeq 0.966$ and $\phi_{\max}^{\text{theoretical}}(Q=20) \simeq 0.901$ from Eq 9. These values are in excellent agreement with the experiments (see Table I). To further validate this idea that $\phi_{\max}$ decreases with the square root of the flow rate, we performed a single experiment at 200 $\mu L/min$ – this leading to a Reynolds number of approximately 30 and thus remaining completely laminar. Results in Fig 8 indicate that the behavior is similar to that of other flow rates, but with a significantly

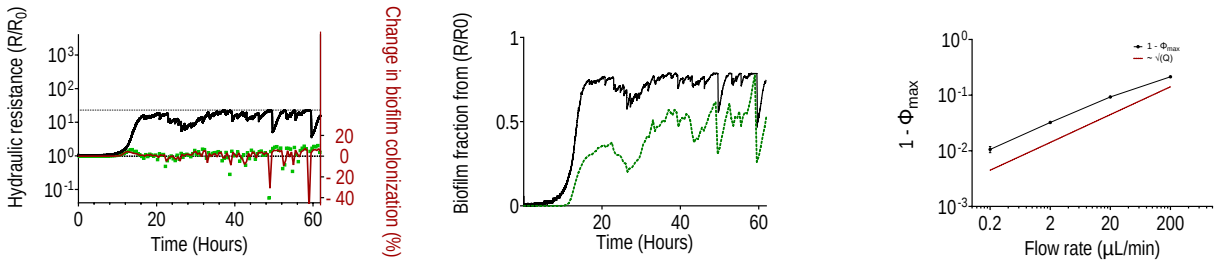

(a) $Q = 200\ \mu L/min$ (b) $Q = 200\ \mu L/min$ (c) $Q = 200\ \mu L/min$

Figure 8: Evolution of $\phi_{\max}$ with the flow rate. (a): Temporal dynamics of the hydraulic resistance for $Q = 200\ \mu L/min$. The figure shows the evolution of the hydraulic resistance (black solid line) in time, calculated from pressure fluctuations. It also shows changes in biofilm colonization extracted from either integrated fluorescence intensity (green squares) or image segmentation (red solid line). (b): Fraction of biofilm in the microchannel, either calculated from hydraulic resistance (black solid line) or estimated from integrated GFP intensity (green dotted line), for the different flow rates. (c): Log-log plot of $1 - \phi_{\max}$ as a function of the flow rate ($Q = 0.2\ \mu L/min$, $2\ \mu L/min$, $20\ \mu L/min$ and $200\ \mu L/min$). The red dotted line simply shows the slope for an evolution with the square root of the flow rate. Error bars represent standard deviation for n = 3 replicates, except for $Q = 200\ \mu L/min$, for which n = 1.

lower value of $\phi_{\max} \simeq 0.786$. We also see that the scaling remains remarkably similar with $1 - \phi_{\max} \sim Q^{\frac{1}{2}}$ in the range $[0.2,\ 200]$ – and therefore, for the hydraulic resistance, we have $\mathcal{R}_{\max} \sim Q^{-1}$ (see Fig S18). The fact that the model can recover the correct scaling suggests that the initial scaling of the detachment rate with the square root of the hydrodynamic stress is correct, which is consistent with previous works [50, 51].

Of course, assuming that $\frac{\chi(Q)}{\chi(Q_{\text{ref}})}\frac{\tau_{\text{reac}}(Q)}{\tau_{\text{reac}}(Q_{\text{ref}})}$ is independent from the flow rate is a strong hypothesis. For the reaction rate, we have previously shown in Section II B 1 that, in the very early stages of adhesion and growth, the doubling times depend on the flow rate – with doubling times for the flow rate 0.2 being significantly larger than for 2 and 20. For the removal rate χ, any change in the composition of the biofilm due to the flow, in particular changes in the extracellular polymeric substances, could modify χ. The model is also based upon several hypotheses, for instance regarding the absence of spatial heterogeneities. Given these limitations, the accuracy of the scaling obtained from the experiments remains remarkable.

5. Sloughing can be described as a stochastic jump process

The model presented so far captures a form of maximum envelope for the biofilm volume fraction. It describes an equilibrium between growth and smooth detachment, in the absence of catastrophic sloughing events. We are now interested in better characterizing and modeling the fluctuations corresponding to sloughing. We first performed a frequency

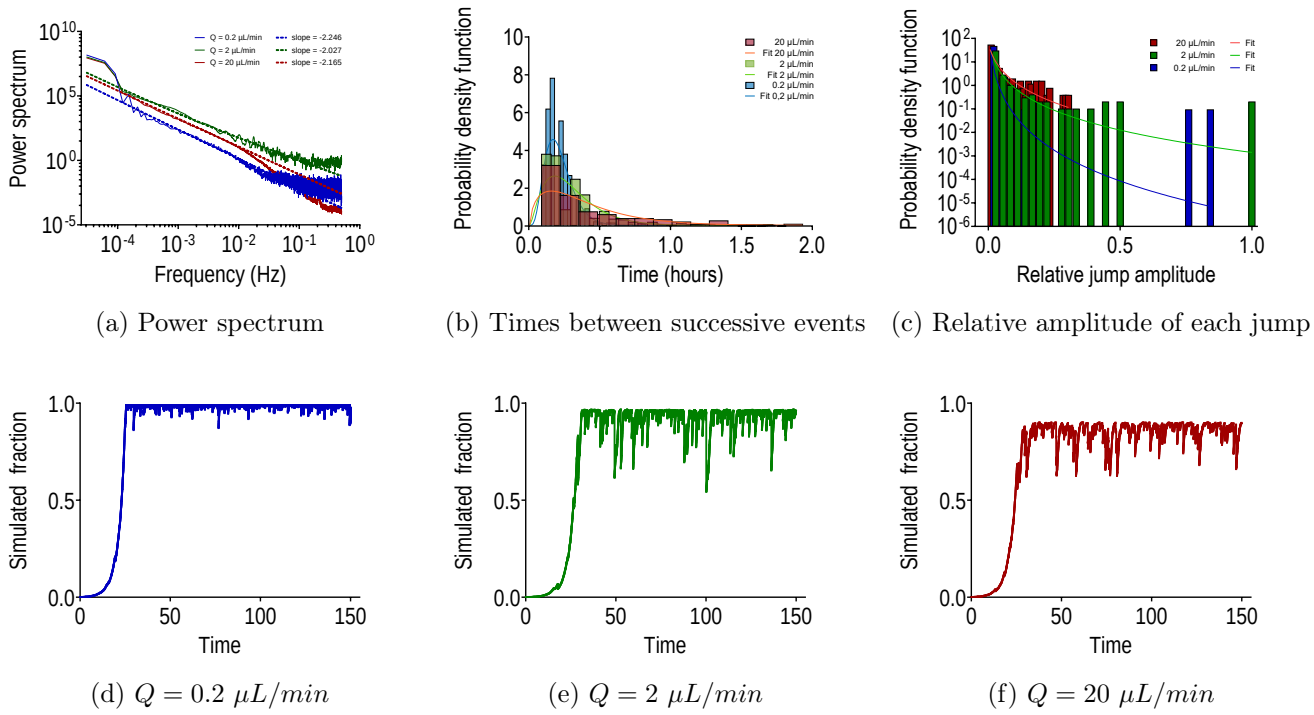

(a) Power spectrum (b) Times between successive events (c) Relative amplitude of each jump

(d) $Q = 0.2\ \mu L/min$ (e) $Q = 2\ \mu L/min$ (f) $Q = 20\ \mu L/min$

Figure 9: Stage II detachment events can be described as a stochastic process. (a) Power spectrum for the different flow rates ($Q = 0.2\ \mu L/min$, $2\ \mu L/min$ and $20\ \mu L/min$). Slopes are indicative and were calculated in the interval between 0 and 0.25 Hz. (b) Probability density function of the time between two successive jump events, δt, for ($Q = 0.2\ \mu L/min$, $2\ \mu L/min$ and $20\ \mu L/min$). The histograms are calculated from experiments, while the solid lines are fitted Gamma distributions $\frac{1}{b^a \Gamma(a)} \delta t^{a-1} e^{-\frac{\delta t}{b}}$. (c) Probability density function of the relative amplitude of jump events, $\xi = \frac{\Delta\phi}{\phi_{t^-}}$, for ($Q = 0.2\ \mu L/min$, $2\ \mu L/min$ and $20\ \mu L/min$). The histograms are calculated from experiments, while the solid lines are fitted log-normal distributions $\frac{1}{\xi\sigma\sqrt{2\pi}} e^{-\frac{(\ln \xi - \mu)^2}{2\sigma^2}}$. (d), (e) and (f): Stochastic simulations of the volume fraction as a function of time for ($Q = 0.2\ \mu L/min$, $2\ \mu L/min$ and $20\ \mu L/min$).

analysis of the signal, as shown in Fig 9a. This approach did not prove very informative as it essentially shows a power spectrum typical of noise, with a slope roughly smaller than -2. This result, however, motivated the construction of a more physical representation. The basis of this representation is the observation that fluctuations have a very specific signature on the hydraulic resistance: they first feature a sharp decrease due to sudden sloughing, followed by a slower increase due to growth. Since growth and smooth biofilm detachment are already described in the model, this observation suggests that we only need to capture the sudden sloughing to improve the description. The model takes the form of the following

stochastic differential equation,

$$d\phi_t = \phi_t \left(1 - \frac{1-\phi_{\max}}{1-\phi_t}\right) dt - \phi_{t^-} dN_t, \tag{10}$$

with ϕ_t describing the average fraction of biofilm in the microchannel, N the jumps and ϕ_{t^-} the value of ϕ at time t^- just before the jump.

The difficult part is to accurately describe the randomness of the process N – which is likely strongly dependent upon spatial heterogeneities, for instance in the initial attachment of bacteria. We characterized N in our experiments via the distributions of both the times between two successive jumps and the relative amplitudes of the jumps – i.e. the amplitude of each jump divided by the value of the volume fraction just before the jump ϕ_{t^-}. Fig 9 shows histograms of these distributions extracted from signal processing of the experimental data (see Material and Methods). We see that the distribution of times between successive jumps, δt, can be well approximated by a Gamma distribution in the form $\frac{1}{b^a \Gamma(a)} \delta t^{a-1} e^{-\frac{\delta t}{b}}$ – solid lines in Fig 9 for a fit of the experimental data. The relative amplitude of each jump $\xi = \frac{\Delta\phi}{\phi_{t^-}}$ was better represented by log-normal distributions of the form $\frac{1}{\xi\sigma\sqrt{2\pi}} e^{-\frac{(\ln\xi-\mu)^2}{2\sigma^2}}$ – solid lines in Fig 9 for a fit of the experimental data. Example realizations of the simulations are presented in Fig 9 for the flow rates used in the experiments. Simulations are strikingly similar to experimental data, thus suggesting that sloughing can indeed be accurately modeled as a stochastic jump process.

6. Flow changes the rheology of the biofilm

Using passive microrheology and multiple particle tracking (MPT) [56–63], we evaluated the role of the hydrodynamic conditions on the viscoelastic properties [64, 65] of the biofilm for three flow rates $Q = 0.2\ \mu L/min$, $2\ \mu L/min$ and $20\ \mu L/min$. The thermally driven motion of $200\,nm$ nanoparticles embedded in the biofilm were tracked, allowing us to calculate the mean square displacement (MSD). Assuming an evolution in time as a power-law, we calculated the exponent α by measuring the slope of the MSD versus time in a log-log plot. The value of α indicates whether the material exhibits normal diffusion ($\alpha = 1$), with particles exhibiting free brownian motion in a purely viscous medium, or subdiffusion ($0 < \alpha < 1$), where the particle motion is hindered. A slope close to 0 would suggest a more solid-like behavior, while a slope close to 1 indicates a more viscous environment. Following the method of Mason et al. [66, 67], we further calculated the shear creep compliance $J(t)$ using the Stokes-Einstein relation.

Results in Fig 10 show that the mechanical properties of the matrix depend on the flow rate. The log-log slope for the MSD (Fig 10a) is similar for all flow rates, with $\alpha \simeq 0.5$. However, the MSD tends to decrease with the flow rate, as is particularly visible on the plots of the creep compliance at $t = 0.1\,s$ (Fig 10b). This suggests that the biofilm becomes

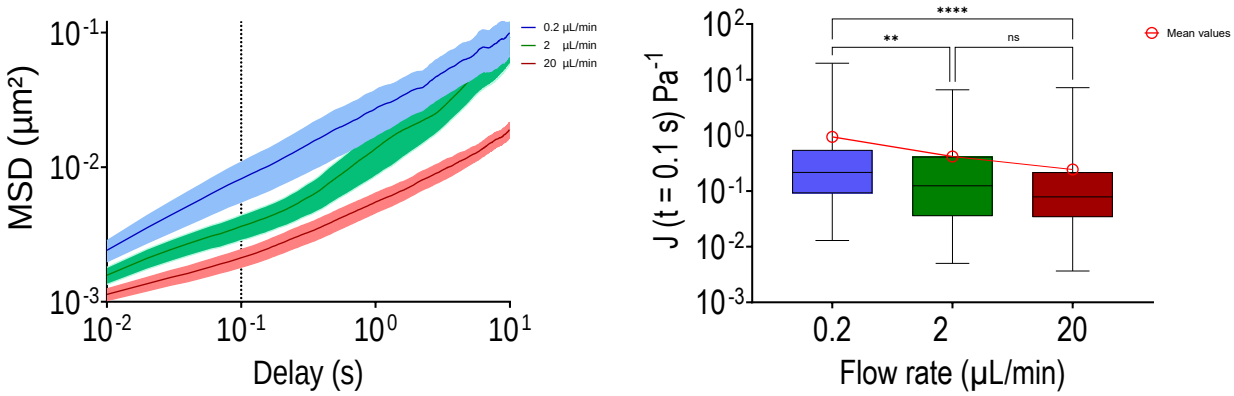

(a) (b)

Figure 10: Changes in the rheology of the biofilm. (a) The ensemble-average mean square displacements for different flow rates ($Q = 0.2\ \mu L/min$, $2\ \mu L/min$ and $20\ \mu L/min$). (b) The shear creep compliance J at t = 0.1 s for each flow rate. For (b), statistical differences were examined by unpaired one-way ANOVA (Kruskal Wallis) with non-Gaussian distribution of data and non-equal SDs. Error bars indicate standard error of mean (SEM) and symbols denote statistical significance (****: p-value <0.0001, **: p-value $= 0.0092$, ns: p-value > 0.05).

less compliant/more rigid with an increase of the flow rate. This idea that larger flows and stresses can lead to the formation of a more compact and stiffer biofilm is consistent with previous studies [68–73]. An intuitive implication is that the biofilm should become more difficult to remove for the largest flow rate and that χ should therefore decrease. This phenomenon could explain, for instance, why there is a cut-off value in the relative amplitude of the jump events at the largest flow rate $20\ \mu L/min$ – contrary to the other flow rates, we observed no sloughing event removing more than 40% of the biofilm in the channel (Fig 9). It may also explain why the distribution of times between detachment events is more heavily tailed towards larger periods Fig 9.

7. Psl are the dominant polysaccharides controlling detachment

Among *P. aeruginosa* PAO1 polysaccharides – Pel, Psl and alginate – Pel and Psl are considered the two primary components of the EPS matrix structure [74], controlling the cohesive and adhesive strength of the biofilm. To determine the role of these polysaccharides on the dynamics, we performed experiments with mutants that cannot produce either Pel or Psl. The Psl mutant is a *pslD* deficient $\Delta pslD$ obtained from *P. aeruginosa* PAO1 by non-polar allelic exchange [75]. The Pel mutant is a pelF deficient strain $\Delta pelF$ also obtained by allelic exchange [76]. Liquid culture showed that the lag and doubling times were, respectively, 233.36 and 105.5 minutes (see Fig S21). Fig 11 (see also S14, S15, S16 and S17) shows the behavior of mutants compared to the wild type. We found that

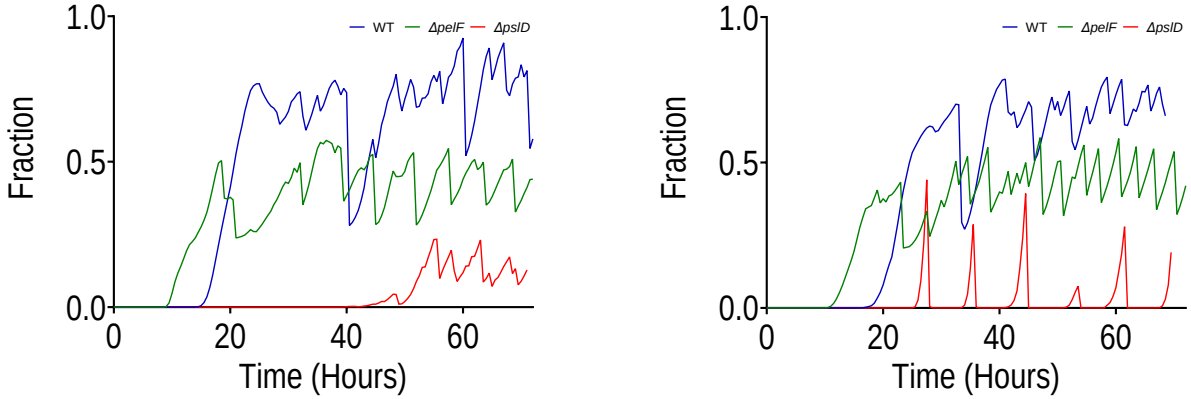

(a) $Q = 0.2\ \mu L/min$ (b) $Q = 2\ \mu L/min$

Figure 11: Fraction of biofilm obtained from image segmentation for the Δpsl (red line) and Δpel strains (green line) compared to the wild-type strain (blue line), for ($Q = 0.2\ \mu L/min$, $2\ \mu L/min$).

the Psl mutant was more strongly affected than the Pel mutant. The Psl mutant only weakly attached to the surface and was more prone to detachment – an observation that is consistent with the prominent role of Psl in the mechanics of PAO1 biofilms [76]. For the case $2\,\mu L/min$, we even observed an almost complete detachment of the biofilm with only few cells remaining attached and making re-growth possible after a sloughing event.

III. DISCUSSION

Among the important factors controlling the development of biofilms, nutrients and oxygen transport plays a central role. Here, we used a nutrient rich medium (brain heart infusion) to study the growth of *P. aeruginosa* PAO1 in various flow conditions in a microchannel. We showed that, for sufficiently low flow rates, growth in the longitudinal direction was limited by the medium – not by oxygen. We modeled transport as an advection-diffusion-reaction transport equation for the limiting molecules, which was characterized by two dimensionless numbers: a Péclet number, Pe, and a Damköhler number, Da, comparing respectively advection to diffusion and reaction to diffusion. Experimentally, we studied the role of these numbers by varying the flow rate, thus the Péclet number, and the inlet nutrient concentration, thus the Damköhler number. We found that the most important dimensionless number is the ratio of the Péclet and Damköhler, $^{Pe}/_{Da}$, comparing advection and reaction. When $^{Pe}/_{Da} < 1$, for the flow rate 0.02 $\mu L/min$, biofilm growth was nutrient-limited and localized close to the inlet. When $^{Pe}/_{Da} > 1$, for flow rates $\geq 0.2\ \mu L/min$, biofilm development was close to homogeneous between the UVC zones, thus indicating that flow is sufficiently efficient to remove nutrient limitations in the longitudinal direction.

We also fitted experimental measurements for the longitudinal distribution of fluorescence to determine the Damköhler number and thus a timescale for the uptake of the limiting nutrient. We found that this timescale was about 100 s for the $1X$ solution of growth medium. Using this information, we also evaluated whether gradients and nutrient limitations could develop in the radial direction of the 100 micrometers channel. Since the timescale for diffusion of nutrients through 50 micrometers of biofilm is only a few seconds, diffusion is much faster than reaction and only weak gradients may develop. Of course, this behavior is highly dependent upon the size of the channel, as the time for diffusion evolves with the square of the characteristic length. For instance, for a channel of 1 mm in size, the diffusion time would be 100 times larger, which would generate strong gradients and potentially radial limitations. Varying the size of the channel may actually represent an interesting way to analyze the effect of gradients and heterogeneities in the radial direction on biofilm development.

Although solute limitation in the longitudinal direction is likely quite a generic feature, the exact component that becomes limiting, in particular whether it is the oxygen or nutrients

for strictly aerobic growth, will depend on the details of the experiment. Using the strain TG1-F' – an *Escherichia coli* K12 derivative carrying a F episome plasmid shown to promote the formation of biofilms Ghigo [77] – Thomen *et al.* [12] found that biofilm growth in a flow chamber was subject to low oxygen levels. The characteristic time for advection of oxygen along their channel (height 250 μm, width 1000 μm, length 3 cm for the flow rate 1 mL/h) is about 30 s, which is similar to the case 0.2 $\mu L/min$ for our 10 mm long channel. If the characteristic times for oxygen consumption are of the same order of magnitude for both bacteria in the different conditions, we could expect to be in similar ranges of $^{Pe}/_{Da}$ for the oxygen with, possibly, longitudinal gradients in our system. However, we did not observe any indication that it was the case or that oxygen played an important role in controlling the growth, which is likely due to important differences between our works.

First, it is possible that there are gradients in our system, but that *P. aeruginosa* responds differently to the low concentration levels. Thomen *et al.* [12] found micro-aerobiosis conditions, not complete depletion, and while *E. coli* can respond strongly to such conditions [78], *P. aeruginosa* is known to be more resilient [79, 80]. Second, it is also possible that we do not have strong longitudinal gradients in our system, either because oxygen uptake is slower or because we better control the boundary conditions of our microchannel. Our system indeed implements a UVC technology to confine bacteria within a specific part of the channel and avoid cross-contamination of the inlet. Biofilm development in the inlet tubing, or before the imaged area, will lead to a reduction of the oxygen concentration in the zone of interest. Lastly, the width and height of our microchannel are different from Thomen *et al.* [12]. Upon considering that there is a central flow channel with a thick layer of biofilm around it, the fact that channels are larger means that the diffusion time through the biofilm is longer. This could generate radial gradients and low oxygen levels close to the boundaries, which may then appear in the transcriptional profiling. Spatially-resolved measurements of oxygen would be extremely valuable to better understand the role of oxygen transport. For example, it would be possible to measure 2D fields of oxygen directly, using either optodes inserted in the chip Ceriotti *et al.* [81] or with the reporter molecule introduced directly in the channel, as in Thomen *et al.* [12], but using lifetime imaging Wu *et al.* [82] to account for local changes in the concentration of the reporter.

Flow acts on the development of the biofilm through two main mechanisms: molecular transport and mechanical stresses. So far in this discussion, we have primarily discussed the

role of nutrient and oxygen transport, but not that of mechanical stresses. To understand the respective role of each of these two mechanisms, an ideal experiment would allow us to probe one mechanism at a time and to establish causal relationships with observations. We therefore attempted to isolate the effect of the mechanical stresses by working at sufficiently high $^{Pe}/_{Da}$, making sure that advection is sufficiently efficient to provide nutrients everywhere in the system. Of course, local concentration gradients, variations in the physico-chemical environments or heterogeneities in the physiological state of the bacteria may persist within the biofilm [83, 84]. But we hypothesized that, when $^{Pe}/_{Da} > 1$, the dominant effect is that of hydrodynamic stresses, not transport limitations.

With that in mind, we then studied the dynamics of the development for flow rates $\geq 0.2\ \mu L/min$. We separated the time response in two stages. Stage I begins just after initial inoculation, as soon as the culture medium starts flowing in the microchannel. Early stage I is dominated by cell adhesion, division, surface motility – the average velocity in the channel at $0.2\ \mu L/min$ is above $300\ \mu m/s$ so bulk motility is likely not playing an important role when $Q \geq 0.2\ \mu L/min$ [54] – and microcolony formation. Stage I then evolved towards the standard steps of biofilm formation for *P. aeruginosa* [1, 85], with first clonal microcolonies that extended, joined together and grew into mature biofilms. The exponential growth and EPS production yielded an increase of the hydraulic resistance of several orders of magnitude, which is consistent with previous works [86, 87]. Curves for the hydraulic resistance then reached an inflection point and were sigmoid-like, which we interpret as a signature of the competition between growth and detachment. Similar regimes to our stage I have been previously described in the literature [88, 89].

Thomen *et al.* [12] found that, for *E. coli* TG1-F', no direct initiation of the biofilm was possible above a shear stress of $10\ mPa$, as cells were only weakly attached to surfaces and easily washed away by the flow. In contrast, our results with *P. aeruginosa* PAO1 show that cells, with shear stress ranging roughly from $2\ mPa$ to $2\ Pa$, strongly adhered to the surface and could initiate biofilm formation in all cases. In fact, most bacteria on most surfaces are able to resist shear stresses far superior to $10\ mPa$ [1, 90–93], often reaching several Pa. We even observed a faster apparent doubling time for the case at $2\ Pa$.

We found another regime in our system, termed Stage II, that was characterized by large fluctuations in the hydraulic resistance and in the quantity of biomass in the channel. We showed that these fluctuations are the result of successive cycles of growth and sloughing

events. Oscillations with sharp changes in the hydraulic resistance were already discussed in several works for biofilm development in porous media. Howell and Atkinson [94] modeled the fluctuations in the effluent concentration and microbial film thickness in trickling filters. Consistent with a number of experimental results, they showed that constant influent concentration and operating conditions can yield large fluctuations induced by sloughing events. [89] studied biofilm development for *Leuconostoc mesenteroides* producing dextran in micromodel experiments with a triangular network of channels linking pore bodies. They found very large oscillations in the pressure signal due to the formation of successive stable or unstable dextran plugs of biofilm, behaving in a way similar to a yield stress fluid, and allowing flow only through breakthrough channels (see detailed discussions on the flow of yield stress fluids through porous media in, for example, [95]). Sharp *et al.* [96] studied the development of *Vibrio fischeri* biofilm in a porous media flat plate reactor. They also showed that "the pore channels are dynamic, changing in sized, number and location with time", due to growth and detachment. Kurz *et al.* [32] studied the development of *Bacillus subtilis* biofilm in a microfluidic system with cylindrical obstacles. They found successive cycles of growth and shear-induced detachment in the preferential flow paths. Bottero *et al.* [97] modeled the coupled effects of flow, clogging and detachment to study the mechanisms that control these self-sustained oscillations, in particular what leads to the clogging of a preferential flow path and the unclogging of another one – contrary to the development of stable flow paths. Although these cycles of growth and detachment have been observed in complex geometries and porous media, it was unclear whether this would apply to a single microchannel, where only one flow path is imposed. We showed that, even in a single channel with continuous flow, these oscillations occur. Our work thus indicates that oscillations due to competitions between growth and hydrodynamic stresses are ubiquitous, affect a broad range of geometries and prevent the system to reach a true steady state. These oscillations may thus play an important role in the development and spreading of biofilms in a range of different applications, such as infections, environmental processes and engineering systems.

We further found that detachment in microchannels is driven by both shear and pressure. Although the role of shear stress is well known in the literature [1, 32, 33, 98, 99], the fact that pressure can trigger detachment has received little attention. In many situations, such as biofilm development in large reactors, shear stress is dominant and the effect of pressure neglected. However, in confined systems, where biofilm can clog a large proportion of the

flow channels, the pressure difference induced by clogging can generate an important force on the biofilm in the direction parallel to the flow. This is the case, for instance, in porous media flows [97]. Other flow systems that involve a form of confinement of the biofilm, such as clogging in pipes, catheters [100] or stents [101], are also directly concerned. A simple approach to quantify this in our system was to estimate the different stresses in the case of uniform film growth between the UVC zones, showing that the contribution of the pressure stress becomes dominant when the volume fraction of biofilm is sufficiently large.

Our results also show that the maximum value of the hydraulic resistance, and the corresponding amount of biomass in the channel, is controlled by an equilibrium between growth and smooth detachment processes. By smooth, we mean all the detachment processes that do not lead to sharp drops in the pressure measurements. Smooth detachment includes mechanisms such as erosion, seeding and biofilm flow outside the zone of interest, but excludes sloughing events. We found that the maximum hydraulic resistance scales with the inverse of the flow rate, which confirms that the rate of detachment scales with the square root of the hydrodynamic stress [49–51]. This result can also be expressed as a critical value of the hydrodynamic stress generating enough detachment to compensate growth. In our framework, this critical stress was in the order of 100-200 Pascals and was independent from the flow rate.

A variety of different meanings have been associated with critical stresses in the literature. Critical stresses have been used to characterize a form of complete detachment from the solid surface [102]. Ohashi and Harada [103] described an adhesion strength as the stress required to remove the biofilm – upon conceptualizing the problem as a surface to surface bonding, the adhesive strength has also be defined as the work required to detach the biofilm from the surface per surface area (in Joule per m^2) [104]. Ohashi and Harada [103] found values for the shear strength in the hundreds of Pascals. Lau *et al.* [105] measured an adhesive pressure – adhesive force measured by microbead force spectroscopy divided by contact area – for *P. aeruginosa* PAO1 that was in the tens of Pascals. Körstgens *et al.* [106] studied the yield strength of a mucoid *P. aeruginosa* strain, discussing its role in the mechanical failure of the biofilm. Considering the biofilm as a viscoelastic gel with plastic flow properties, they found a stress at failure close to 1000 Pa. Lee *et al.* [107] show that bio-aggregates of *E. coli* at pore throats become fluidized above a critical value of the shear stress with a yield point at roughly 1.8 Pa. It is difficult to reconcile these different measurements, as they have

different physical meanings and are obtained for different bacteria, using different methods in different conditions. However, they indicate that values in the range 100-200 Pascals for an equilibrium between growth and detachment for *P. aeruginosa* are not unreasonable.

Microrheology measurements of the viscoelastic properties of the biofilm also revealed that the biofilm grown at larger flow rates were stiffer. This behavior is consistent with several studies from the literature [15, 73, 108, 109]. Intuitively, one would think that this should have a direct impact on detachment – with biofilm being tougher to completely remove for the largest flow rate – and it is possible that we are seeing this effect in the probability density functions characterizing sloughing. However, this is not completely straightforward. We have seen, for instance, that the critical value of the stress for which smooth detachment equilibrates growth did not seem to depend upon the flow rate. To our knowledge, establishing a clear link between rheological properties and detachment remains an open problem. Progressing in that direction requires a better comprehension of how the different modes of detachment occur – for example, for sloughing, does the biofilm detach from the surface or does it break within the matrix? It also requires a better understanding of the role of adhesive forces to the surfaces, the respective influence of viscosity and elasticity, and perhaps the most important how bacteria actively regulate detachment, for instance through quorum sensing [110] or rhamnolipids production [111].

The two main exopolysacharides produced by nonmucoid strains of *P. aeruginosa* are Psl and Pel. In our work, we used Δpsl and Δpel mutants to assess the role of each one on the spatio-temporal dynamics of the development. We found that Psl is the primary exopolysacharides controlling detachment. For the Δpsl mutant, we observed major sloughing events for 2 $\mu L/min$ and a complete removal for 20 $\mu L/min$. The dynamics of sloughing was also affected, suggesting that Psl plays an important role in all modes of biofilm detachment. On the other hand, Pel featured a dynamics similar to that of the wild type, but with a reduced quantity of biomass.

A fundamental aspect of our work is the quantitative analysis of the data performed through mathematical modeling of the different processes. It is important to note that, in order to proceed with this analysis, a precise control of environmental and boundary conditions is needed. Our microfluidic system, combined with a UVC device to contain the biofilm in a specific zone of the channel, made this possible. Our approach to modeling was constructed in two main parts. We first proposed differential equations to describe nutrient

transport coupled with the dynamics of biofilm development in the channel, including growth and smooth detachment. The sharp jumps corresponding to sloughing were then added to this first layer of the model as a jump stochastic process. One of the advantages of the stochastic description is that we could avoid a full two or three-dimensional description of biofilm development [112] in the channel. The gain in complexity and computation cost could help model large systems, such as porous media.

Although it seems quite natural to characterize the statistics of detachment [113], there are actually very few attempts to treat such problems in the framework of stochastic processes. Howell and Atkinson [94] modeled sloughing in trickling filters through a conceptualization as connected filter units describing the discrete pieces of packing material in the filter. They introduced randomness of sloughing times by permitting sloughing at multiples of a fixed time interval. Bohn *et al.* [114] used an approach combining a logistic growth with random sloughing events through a stochastic differential equation. They described sloughing via a discrete expression of the amplitude of jumps occurring independently at each time step, which allowed them do describe daily fluctuations in light absorbance data for phototrophic biofilms development in a flow-lane incubator. In our approach, the jump process was characterized by two random variables: the interevent time between two successive jumps and the relative amplitudes of the jumps. Through the analysis of experimental data, we reconstructed the probability density functions for these random variables, with respectively Gamma and log-normal distributions.

There have been previous discussions [115] on the determinism of biofilm formation, suggesting that sloughing events are intrinsically random events that generate large fluctuations, prevent the system from reaching a steady state and hinder the reproducibility of long-term experiments. Our work confirms that sloughing is integral to biofilm development [33] but shows that, although a true steady state is never reached, the fluctuations can be precisely characterized using stochastic modeling. This approach paves a way forward in terms of reproducibility: even though the state of the biofilm at any given time may not be reproducible, the randomness of the process may very well be.

Our approach to characterizing bursting events in terms of the distribution of the amplitude and interevent time is reminiscent of the description of other physical systems, such as avalanches [116]. For earthquakes, for example, a Gamma distribution for interevent times has been found in many different geographic regions [117]. The fact that interevent

times for biofilm sloughing also seem to follow a Gamma distribution may point towards specific physical mechanisms [118], which could be used to better understand the physics of sloughing. One interesting perspective of this work is also to assess the universality of these distributions across microorganisms and whether we could define classes of bacteria with specific signatures on the stochastic process. With the same idea, we could further evaluate the impact of ecological interactions in multispecies biofilm or the effect of various biocides, antibiotics or quorum-sensing inhibitors on the sloughing dynamics.

IV. MATERIAL AND METHODS

A. Bacteria and cultures

Experiments were performed using *Pseudomonas aeruginosa* PAO1 GFP (ATCC 15692GFP) strain, along with PAO1 GFP $\Delta pslD$ and $\Delta pelF$ mutants obtained from Colvin *et al.* [75, 76] and built by non-polar deletion through allelic replacement of *pslD* and *pelF* operon and harbor pMRP9-1 plasmid expressing GFP. Bacteria were subcultured and grown in brain heart infusion (Sigma Aldrich, Saint-Quentin-Fallavier, France). Cultures were prepared from -80°C frozen aliquots spread on tryptic soy agar plate (Sigma Aldrich, Saint-Quentin-Fallavier, France) supplemented with 300 µg/mL of ampicillin (Sigma Aldrich) then incubated at 30°C during 24 h. Liquid cultures were prepared from the second subcluture on tryptic soy agar by spreading a 24 hours single colony diluted in brain heart infusion media supplemented with 300 µg/mL of ampicillin. $1X$ concentrated BHI media was prepared by dissolving $37\,g$ of commercial powder in demineralized water and autoclaved with a liquid cycle (121° C for 15 minutes). $0.2X$concentrated BHI media was obtained by dissolving $7.4\,g$ while a third $1X$ solution was supplemented by $8\,g/L$ of D-Glucose (Sigma Aldrich).

B. Microfabrication

Microchannels were fabricated using standard soft lithography techniques. Microchannel molds were prepared by depositing 100 µm SUEX sheets on a silicium wafer via photolithography. The negative mold was cleaned by isopropanol and silanized with trichloromethylsilane (Sigma Aldrich). Square cross-section channels had dimensions of 100 µm height by 100 µm width and 20 mm length. The chips were prepared with a 10% wt/wt cross-linking agent in the polydimethylsiloxane solution (Sylgard 184 Silicone Elastomer Kit, Dow Corning). PDMS was cleaned with isopropanol at 80 °C for 30 minutes and plasma-bonded to a clean glass coverslide.

C. Inoculation and flow experiments

BHI suspensions were adjusted at optical density at $OD_{620\,nm}$= 0.2 ($10^8\,CFU/mL$) and inoculated inside the microchannels from the outlet, up to approximately ¾ of the channel length in order to keep a clean inlet. The system was let at room temperature (25°C) for 3h under static conditions. Flow experiments were then performed at $0.02, 0.2, 2, 20$ and 200 $\mu L/min$ constant flow rates for 72h in the microchannels at room temperature. For the experiments at $0.2, 2, 20$ and 200 $\mu L/min$, the fluidic system was based on a sterile culture medium reservoir pressurized by a pressure controller (Fluigent FlowEZ) and connected with a flow rate controller (Fluigent Flow unit). The flow rate was maintained constant by using a controller with a feedback loop adjusting the pressure in the liquid reservoir. The reservoir was connected to the chip using Tygon tubing (Saint Gobain Life Sciences Tygon™ ND 100-80) of 0.52 mm internal diameter and 1.52 mm external diameter, along with PEEK tubing

(Cytiva Akta pure) with 0.25 mm inner diameter adapters for flow rate controller. The waste container was also pressurized by another independent pressure controller to reduce air bubble formation in the inlet part. For the experiments at 0.02 $\mu L/min$, we used an Harvard Phd2000 syringe pump for the flow.

D. UVC irradiation

The inlet and outlet of the microchannels were exposed to UVC light by a system of UVC LEDs [44] to avoid biofilm formation in inlet and outlet part. The system consists of a 3D printed part called the guide carrying in its backside a PCB with a LED light source that delivers UV-C light of 1W power. The light beam follows a straight trajectory until a 45° mirror positioned in the front side of the guide, which reflects the light parallel to the PDMS chip and irradiate it. UVC guides were positioned in both sides of the PDMS microchannel and separated by a 1.2 cm distance to keep a central area unexposed. UVC power is measured by a radiometer after mirror reflection and delivers a power of $200\,mW/m^2$equivalent to $2\,mJ/cm^2$. The guide is elevated to fit with the PDMS chip dimensions and contains a barrier located in the front side that blocks the diffusion of light through the PDMS polymer in the horizontal direction.

E. Mass spectrometry analysis

Mass spectrometry analysis was performed on a Thermo Scientific Q Exactive Focus Orbitrap LC-MS/MS system connected to a LC device Thermo Scientific Vanquish UPLC system with PDA detection. Analytical separations were performed on a 150 x 2.1 mm Thermo Hypersyl Gold C18 column (1.9 µm) using an MeCN/H2O 1% formic acid gradient. Data were captured in full MS scan mode and processed using Chromeleon 7 software.

F. Imaging for the biofilm experiment

Bacterial development was imaged for a period of 72 hours with a timestep of 30 minutes at 25°C on an inverted microscope (Ti-2E, Nikon) using a digital camera (back-illuminated PCO edge). Timelapse images were acquired using brightfield and fluorescence microscopy (Sola light source 10% intensity with 30 ms exposure with $500\,nm$ excitation and $513\,nm$ emission combined with (FITC filter). Images were obtained with a focal plan at the glass/liquid interface. These images had dimensions of 30086 x 154 pixels obtained after multi position scanning using automatic Nikon platform and assembled by Nikon NIS software of single images with 0.65 µm/pixel using a 10X magnification Nikon objective (NA = 0.3).

G. Image analysis for the biofilm distribution in the longitudinal direction

Fluorescence images were loaded as a matrix (30086 x 154) in MATLAB (MathWorks). For each time acquisition, the signal was first integrated in the radial direction to obtain a mean distribution in the longitudinal direction. In plotting curves to analyze the effect of nutrients, all timepoints were then averaged to obtain one dimensional curves of the mean longitudinal profile. For kymographs, one dimensional curves for each time point were stacked together to describe the spatio-temporal dynamics. The intensity values were normalized to the maximum values of each replicate over all times. For each flow and nutrient condition, three biological replicates were performed.

H. Image analysis for the biofilm segmentation

To estimate changes in channel colonization, GFP images were binarized using a machine learning software (Ilastik) [119]. Images were pre-treated with imageJ [120] by normalizing all pixel values between 0 and 65535 grayscale levels. In Ilastik, biofilm structures were first differentiated from the empty flow path using pixel-level manual labeling during pixel classification where visible patches of biofilm and empty channel were annotated manually by mouse cursor. Pixel classification workflow employs a Random Forest classifier, known for its generalization properties. Several samples of biofilm and background images were used to train the classifier by annotating pixels with corresponding labels, allowing the algorithm to learn and make predictions in real-time. The chosen features were color, intensity, edges, and texture. The generated probability maps indicating the likelihood of each class at every pixel were used for the object classification and were thresholded at a value of 0.6 with no size filter. Thresholding is a process involved in converting continuous probability maps generated from pixel classification into binary segmentation images by setting a threshold, where pixels above the threshold are classified as belonging to an object. The size, intensity, position and convexity of the biofilm objects was exported in .cvs format and further analysed in matlab. Volumic fraction of biofilm in microchannel was calculated from the sum of the size of segmented objects divided by the interest growth area (non UVC irradiated central part of microchannel).

I. Initial adhesion

Separate experiments were performed to study the behavior of cells in the initial phases of attachment in order to increase spatial and temporal resolution. Liquid cultures were prepared following the same protocol as described previously (IV C). Sterile 1× concentrated

BHI culture medium supplemented by $300\,\mu g/mL$ of ampicillin was flowed under constant flow rate ($Q = 0.2\ \mu L/min$, $2\ \mu L/min$ and $20\ \mu L/min$) after 3 hours under static conditions at 26° C.

Images were obtained with a 40× Nikon objective (NA = 0.95) using a differential interference contrast (DIC) brightfield with 2 minutes per frame during 3.5 Hours. Replicates were obtained by imaging four positions per channel and each condition was performed in two distinct channels forming two distinct biological replicates to obtain n = 8 replicates by condition ($Q = 0.2\ \mu L/min$, $2\ \mu L/min$ and $20\ \mu L/min$). The images were further segmented using Ilastik with the same parameters as described before and single cells were selected as objects with an area higher than $20\,\mu m^2$ to avoid counting dust particles and artefacts that could be considered as distinct objects by Ilastik. The doubling time was calculated in the window between 0 and 3.5 hours by a a linear fitting of the logarithm of the number of cells. The slope was used to estimate growth rate and doubling time. Cell count was calculated from image segmentation of four positions in two channels to generate 8 replicates by condition (n= 8) for ($Q = 0.2\ \mu L/min$, $2\ \mu L/min$ and $20\ \mu L/min$).

J. Wavelet analysis

Time series of the pressure data were investigated with a wavelet analysis to identify temporal variations of spectral power [121]. Wavelet analysis was carried out using a Morlet wavelet, the product of a sinusoidal wave and a Gaussian envelope, with a frequency parameter of 6 and scale width of 300. We then applied a continuous wavelet transform (CWT) results which gives wave power coefficients dependent on the scale or period and the time, as well as a cone of influence (COI), where edge effects become important. The time series were zero-padded to reduce the edge errors. The cone of influence was removed from the scalograms in Fig 3.

K. Data analysis for the calculation of the hydraulic resistance and volume fraction

Recorded pressure fluctuations in the reservoir were converted to hydraulic resistance in the 10 mm zone between UVC LEDs where biofilm develops. We write the difference between the two pressure reservoirs (one at the inlet and one at the outlet) as ΔP_{res} and express it as

$$\Delta P_{\text{res}}(t) = \left(\sum_i R_i + R(t) \right) Q$$

with Q the imposed flow rate, $\sum_i R_i$ the sum of the hydraulic resistance of the different part of the hydraulic network and $R(t)$ the hydraulic resistance of the the 10 mm zone between UVC LEDs. To estimate $R(t)$, we evaluated $\sum_i R_i$ from the mean value of ΔP_{res}, which we write $\overline{\Delta P}_{\text{res}}$, over a few hours of the experiment where biofilm growth is not yet observable. We then use

$$\sum_i R_i = \frac{\overline{\Delta P}_{\text{res}}}{Q} - R(t=0),$$

which yields

$$\frac{R(t)}{R(t=0)} = 1 + \frac{\Delta P_{\text{res}}(t) - \overline{\Delta P}_{\text{res}}}{Q\ R(t=0)},$$

with $R(t=0)$ in the square cross-section of size $h_0 = 100\ \mu m$ that can be estimated as

$$R(t=0) \simeq \frac{12\eta L}{1 - 0.917 \times 0.63} \frac{1}{h^4}$$

with η the viscosity of the culture medium at 25°C, $L = 10\ mm$ the length of the channel and h the width/height of the channel. Since we considered $\overline{\Delta P}_{\text{res}}$ for the normalization, and because the low pressure signal is relatively noisy at the beginning, we also only use the part of the signal for which $\frac{R(t)}{R(t=0)} \geq 1$ – it is a important, for instance, to obtain non-negative volume fractions of biofilm that are only the result of the initial noise. Upon assuming that the biofilm forms a uniform layer on the sides of the channel (see schematics in Fig S1), we also have

$$\frac{R(t)}{R(t=0)} = \left(\frac{h}{h-2b}\right)^4,$$

with b the thickness of the biofilm layer. The volume fraction of biofilm is $\phi = 1 - \left(\frac{h-2b}{h}\right)^2$ so that

$$\phi = 1 - \sqrt{\frac{R(t=0)}{R(t)}}.$$

L. Frequency analysis

Welch power spectral analysis [122] of the pressure signal was carried out by dividing the time signal into smaller segments, calculating their periodogram and finally averaging accross the frequencies, resulting in a power spectral density (PSD) estimate. This method allows for PSD estimate that is less noisy than usual periodograms. Here, we used the Matlab tool pwelch to estimate the PSD using hanning window with an overlap of 50%. A linear fit was then applied on the interval in the low frequency range.

M. Microrheology

Mechanical properties of the biofilm were determined using a passive microrheology method. This approach uses multiple particle tracking (MPT) to monitor the thermally driven motion of fluorescently labeled probe particles within the biofilm. Specifically, carboxylated red fluorescent nanoparticles with a diameter 200 nm (F8810, Invitrogen) were diluted in the bacterial culture prior to the experiment (0.25% v/v) . After 48h under different flow rates(Q = 0.2 µL/min, 2 µL/min and 20 µL/min), imaging was carried out using a high-speed camera (pco.DIMAX) attached to an inverted epifluorescence microscope (Ti2-E, Nikon) with a 40X objective (NA = 0.95) and a SOLA light source combined with a TRITC filter. Movies were recorded at various locations of the microfluidic channels at a constant height (center region of the biofilm) for 30 seconds at the fast rate of 100 frames per second at room temperature. A total of three replicates was done for each flow rate condition with a total number of nanoprobes 347 -517 - 1229 for Q = 0.2 µL/min, 2 µL/min and 20 µL/min respectively. Only probes with trajectories having more than 1000 frames were taken into account for further analysis.

Recorded movies were post-processed using Fiji by subtracting the background noise and by correcting the unevenness with a rolling ball of 50 pixels. Areas with high biofilm autofluorescence were masked to avoid potential tracking inaccuracies. A homemade Matlab code, inspired from [123, 124], was then used to reconstitute the probe trajectories with a subpixel local nearest-neighbour linking of the particles in each frame. The 2D mean-squared displacement (MSD) for each particle was computed as $\langle \Delta r^2(\tau) \rangle = \left\langle [r(t+\tau) - r(t)]^2 \right\rangle$, where τ is the lag time. For viscoelastic materials, the MSD measured in 2D follows a power-law $\langle \Delta r^2(\tau) \rangle \propto \tau^\alpha$ where values of $\alpha = 0$ indicate immobile behavior, thus a rigid environment while $\alpha = 1$ indicate a purely viscous material and values $0 < \alpha < 1$ indicate a subdiffusive behavior in a viscoelastic environment. MSD plots as a function of τ were analyzed by a weighted fit of the subdiffusion (10% of the lag times were taken into account) and only slopes α between the values of 0 and 1 were considered for further analysis [125]. Only fits with quality of fit $R^2 > 0.96$ were kept into consideration with a final total of probes N = 78 - 97 - 258 for Q = 0.2 µL/min, 2 µL/min and 20 µL/min respectively.

Particle motion can then be linked to rheological properties, such as the shear creep compliance $J(t)$ which estimates how a material deforms under constant stress over time. Using the Mason and Weitz method [126, 127] and the Generalized Stokes-Einstein Relation (GSER), J can be written as

$$J(t) = \frac{3\pi a}{2k_B T} \left\langle \Delta r^2(t) \right\rangle \tag{11}$$

where a is the particle radius, k_B the Boltzmann constant and T the temperature (T=298K). Values of creep compliance at t=0.1s were calculated for each particle.

Q	a	b	μ	σ
0.2 $\mu L/min$	3.71	7.28×10^{-2}	-5.19	1.28
2 $\mu L/min$	3.51	8.90×10^{-2}	-5.07	1.29
20 $\mu L/min$	1.53	2.50×10^{-1}	-3.90	1.34

Table II: Values obtained from direct fitting of the experimental data

N. Construction of the probability density functions for jumps and fits

Volume fraction data were processed using a homemade Matlab code. Each dataset was first subsampled by keeping only 1 in 150 points. The subsampled signal was then differentiated and only negative values corresponding to detachment events were conserved. Jumps were then identified through the selection of local maxima. For each flow rate, all the values for the times between two successive jumps and the relative amplitude of the jumps – amplitude of the jump relative to the value of the volume fraction just before the jump – for the different replicates were aggregated to construct the distributions.

Gamma distributions were then fitted to the experimental data for the times between successive jumps and lognormal distributions were used for the amplitude of the jumps. Values for the different parameters are summarized in Table.II.

O. Numerical simulation of the stochastic process

Here we describe how we simulated the evolution of the volume fraction ϕ, solving

$$d\phi_t = \phi_t \left(1 - \frac{1-\phi_{\max}}{1-\phi_t}\right) dt - \phi_{t^-} dN_t. \tag{12}$$

The simulation was done using a homemade Matlab code. For each case, based on the previously calculated distributions, we first generated two sets of random numbers corresponding to the times between successive jumps and to the relative amplitude of the jumps – therefore allowing us to completely determine the jump process, N. We then simply solved the ordinary differential equation

$$\dot{\phi} = \phi \left(1 - \frac{1-\phi_{\max}}{1-\phi}\right), \tag{13}$$

between jumps using the Matlab solve ode45. Upon reaching a jump, the simulation was stopped and the jump implemented, before proceeding to treating the next interval.

P. Comsol flow simulations

Flow simulation was performed using a finite element approach in Comsol v6.1. The channel was treated as a rectangle of $850\,\mu m$ length by $100\,\mu m$ width. Biofilm, as shown in white in Fig 5, was added from a segmentation of real experimental images. We then solved incompressible Stokes flow with no-slip/no-penetration boundary conditions on the solid and on the biofilm surface. The inlet condition was an imposed velocity, while the outlet was an imposed pressure.

ACKNOWLEDGMENTS

This work is part of a project that has received funding from the European Research Council (ERC) under the European Union's Horizon 2020 research and innovation programme (grant agreement no 803074). This work was partially supported by the LAAS-CNRS micro and nanotechnologies platform, a member of the French Renatech network. We thank the entire BEBOP team for daily interactions and assistance; Julien Lefort and Emmanuel Libert for their technical support; Terence Desclaux for the introduction to wavelet analysis; Matthew R. Parsek and Maria Zori for providing the Pel and Psl mutants; and Laure Latapie for her support with mass spectrometry.

---

[1] M. Krsmanovic, D. Biswas, H. Ali, A. Kumar, R. Ghosh, and A. K. Dickerson, Hydrodynamics and surface properties influence biofilm proliferation, Advances in Colloid and Interface Science **288**, 102336 (2021).

[2] H. J. Busscher and H. C. van der Mei, Microbial Adhesion in Flow Displacement Systems, Clinical Microbiology Reviews **19**, 127 (2006).

[3] C. A. Rodesney, B. Roman, N. Dhamani, B. J. Cooley, P. Katira, A. Touhami, and V. D. Gordon, Mechanosensing of shear by Pseudomonas aeruginosa leads to increased levels of the cyclic-di-GMP signal initiating biofilm development, Proceedings of the National Academy of Sciences **114**, 5906 (2017).

[4] S. Wang, H. Zhu, G. Zheng, F. Dong, and C. Liu, Dynamic Changes in Biofilm Structures under Dynamic Flow Conditions, Applied and Environmental Microbiology **88**, e01072 (2022).

[5] T. J. Battin, K. Besemer, M. M. Bengtsson, A. M. Romani, and A. I. Packmann, The ecology and biogeochemistry of stream biofilms, Nature Reviews Microbiology **14**, 251 (2016).

[6] Y. F. Dufrêne and A. Persat, Mechanomicrobiology: How bacteria sense and respond to forces, Nature Reviews Microbiology **18**, 227 (2020).

[7] I. Sampedro, R. E. Parales, T. Krell, and J. E. Hill, *Pseudomonas* chemotaxis, FEMS Microbiology Reviews , n/a (2014), chemotaxis Positive and negative.

[8] J. E. Sanfilippo, A. Lorestani, M. D. Koch, B. P. Bratton, A. Siryaporn, H. A. Stone, and Z. Gitai, Microfluidic-based transcriptomics reveal force-independent bacterial rheosensing, Nature Microbiology **4**, 1274 (2019).

[9] J. W. Costerton, Z. Lewandowski, D. E. Caldwell, D. R. Korber, and H. M. Lappin-Scott, Microbial biofilms, Annual Review of Microbiology **49**, 711 (1995).

[10] H.-C. Flemming, J. Wingender, U. Szewzyk, P. Steinberg, S. A. Rice, and S. Kjelleberg, Biofilms: An emergent form of bacterial life, Nature Reviews Microbiology **14**, 563 (2016).

[11] H.-C. Flemming and J. Wingender, The biofilm matrix, Nature Reviews Microbiology **8**, 623 (2010).

[12] P. Thomen, J. Robert, A. Monmeyran, A.-F. Bitbol, C. Douarche, and N. Henry, Bacterial biofilm under flow: First a physical struggle to stay, then a matter of breathing, PLoS ONE **12**, e0175197 (2017).

[13] R. Rusconi, S. Lecuyer, N. Autrusson, L. Guglielmini, and H. A. Stone, Secondary Flow as a Mechanism for the Formation of Biofilm Streamers, Biophysical Journal **100**, 1392 (2011).

[14] K. Besemer, G. Singer, R. Limberger, A.-K. Chlup, G. Hochedlinger, I. Hödl, C. Baranyi, and T. J. Battin, Biophysical Controls on Community Succession in Stream Biofilms, Applied and Environmental Microbiology **73**, 4966 (2007).

[15] P. Stoodley, I. Dodds, J. Boyle, and H. Lappin-Scott, Influence of hydrodynamics and nutrients on biofilm structure, Journal of Applied Microbiology **85**, 19S (1998).

[16] B. W. Peterson, Y. He, Y. Ren, A. Zerdoum, Matthew R. Libera, P. K. Sharma, A.-J. van Winkelhoff, D. Neut, P. Stoodley, H. C. van der Mei, and H. J. Busscher, Viscoelasticity of biofilms and their recalcitrance to mechanical and chemical challenges, FEMS microbiology reviews **39**, 234 (2015).

[17] E. S. Gloag, S. Fabbri, D. J. Wozniak, and P. Stoodley, Biofilm mechanics: Implications in infection and survival, Biofilm **2**, 100017 (2020).

[18] D. Taherzadeh, C. Picioreanu, and H. Horn, Mass Transfer Enhancement in Moving Biofilm Structures, Biophysical Journal **102**, 1483 (2012).

[19] C. Picioreanu, M. C. Van Loosdrecht, and J. J. Heijnen, Effect of diffusive and convective substrate transport on biofilm structure formation: A two-dimensional modeling study, Biotechnology and Bioengineering **69**, 504 (2000).

[20] M. K. Kim, F. Ingremeau, A. Zhao, B. L. Bassler, and H. A. Stone, Local and global consequences of flow on bacterial quorum sensing, Nature Microbiology **1**, 15005 (2016).

[21] P. Emge, J. Moeller, H. Jang, R. Rusconi, Y. Yawata, R. Stocker, and V. Vogel, Resilience of bacterial quorum sensing against fluid flow, Scientific Reports **6**, 33115 (2016).

[22] S. Mukherjee and B. L. Bassler, Bacterial quorum sensing in complex and dynamically changing environments, Nature Reviews Microbiology **17**, 371 (2019).

[23] J. C. Conrad and R. Poling-Skutvik, Confined Flow: Consequences and Implications for Bacteria and Biofilms, Annual Review of Chemical and Biomolecular Engineering **9**, 175 (2018), _eprint: https://doi.org/10.1146/annurev-chembioeng-060817-084006.

[24] B. E. Rittmann, The significance of biofilms in porous media, Water Resources Research **29**, 2195 (1993).

[25] S. W. Taylor and P. R. Jaffé, Biofilm growth and the related changes in the physical properties of a porous medium: 1. Experimental investigation, Water Resources Research **26**, 2153 (1990), _eprint: https://agupubs.onlinelibrary.wiley.com/doi/pdf/10.1029/WR026i009p02153.

[26] S. W. Taylor, P. C. D. Milly, and P. R. Jaffé, Biofilm growth and the related changes in the physical properties of a porous medium: 2. Permeability, Water Resources Research **26**, 2161 (1990).

[27] S. W. Taylor and P. R. Jaffé, Biofilm growth and the related changes in the physical properties of a porous medium: 3. Dispersivity and model verification, Water Resources Research **26**, 2171 (1990).

[28] S. W. Taylor and P. R. Jaffé, Substrate and biomass transport in a porous medium, Water Resources Research **26**, 2181 (1990).

[29] P. Vandevivere and P. Baveye, Saturated Hydraulic Conductivity Reduction Caused by Aerobic Bacteria in Sand Columns, Soil Science Society of America Journal **56**, 1 (1992).

[30] P. Vandevivere and P. Baveye, Effect of bacterial extracellular polymers on the saturated hydraulic conductivity of sand columns, Applied and Environmental Microbiology **58**, 1690 (1992).

[31] K. Drescher, Y. Shen, B. L. Bassler, and H. A. Stone, Biofilm streamers cause catastrophic disruption of flow with consequences for environmental and medical systems, Proceedings of the National Academy of Sciences **110**, 4345 (2013).

[32] D. L. Kurz, E. Secchi, F. J. Carrillo, I. C. Bourg, R. Stocker, and J. Jimenez-Martinez, Competition between growth and shear stress drives intermittency in preferential flow paths in porous medium biofilms, Proceedings of the National Academy of Sciences **119**, e2122202119 (2022).

[33] U. Telgmann, H. Horn, and E. Morgenroth, Influence of growth history on sloughing and erosion from biofilms, Water Research **38**, 3671 (2004).

[34] T. L. Stewart and H. S. Fogler, Biomass plug development and propagation in porous media, Biotechnology and Bioengineering **72**, 353 (2001).

[35] J. Verran, Biofouling in Food Processing: Biofilm or Biotransfer Potential, Food and Bioproducts Processing **80**, 292 (2002).

[36] M. Aslam, R. Ahmad, and J. Kim, Recent developments in biofouling control in membrane bioreactors for domestic wastewater treatment, Separation and Purification Technology **206**, 297 (2018).

[37] M. Cowle, A. Babatunde, W. Rauen, B. Bockelmann-Evans, and A. Barton, Biofilm development in water distribution and drainage systems: Dynamics and implications for hydraulic efficiency, Environmental Technology Reviews **3**, 31 (2014).

[38] S. García and A. Trueba, Fouling in Heat Exchangers, in *Inverse Heat Conduction and Heat Exchangers*, edited by S. Bhattacharya, M. Moghimi Ardekani, R. Biswas, and R. C. Mehta (IntechOpen, 2020).

[39] G. Bixler and B. Bhushan, Review article: Biofouling: Lessons from nature, Philosophical transactions. Series A, Mathematical, physical, and engineering sciences **370**, 2381 (2012).

[40] R. Singh, D. Paul, and R. K. Jain, Biofilms: Implications in bioremediation, Trends in Microbiology **14**, 389 (2006).

[41] R. Sen, Biotechnology in petroleum recovery: The microbial EOR, Progress in Energy and Combustion Science **34**, 714 (2008).

[42] Y. Kryachko, Novel approaches to microbial enhancement of oil recovery, Journal of Biotechnology **266**, 118 (2018).

[43] J. Lennox and J. Ashe, Biofilms as Biobarriers, The American Biology Teacher **71**, 20 (2009).

[44] G. Ramos, C. Toulouze, M. Rima, O. Liot, P. Duru, and Y. Davit, Ultraviolet control of bacterial biofilms in microfluidic chips, Biomicrofluidics **17**, 024107 (2023).

[45] S. Arat, G. S. Bullerjahn, and R. Laubenbacher, A Network Biology Approach to Denitrification in Pseudomonas aeruginosa, PLoS ONE **10**, e0118235 (2015).

[46] M. D. Bartberger, W. Liu, E. Ford, K. M. Miranda, C. Switzer, J. M. Fukuto, P. J. Farmer, D. A. Wink, and K. N. Houk, The reduction potential of nitric oxide (NO) and its importance to NO biochemistry, Proceedings of the National Academy of Sciences **99**, 10958 (2002).

[47] J. P. Folsom, L. Richards, B. Pitts, F. Roe, G. D. Ehrlich, A. Parker, A. Mazurie, and P. S. Stewart, Physiology of Pseudomonas aeruginosa in biofilms as revealed by transcriptome analysis, BMC Microbiology **10**, 294 (2010).

[48] H. Bruus, *Theoretical Microfluidics* (OUP Oxford, 2008).

[49] K. Z. Coyte, H. Tabuteau, E. A. Gaffney, K. R. Foster, and W. M. Durham, Microbial competition in porous environments can select against rapid biofilm growth, Proceedings of the National Academy of Sciences **114**, E161 (2017).

[50] R. Duddu, D. L. Chopp, and B. Moran, A two-dimensional continuum model of biofilm growth incorporating fluid flow and shear stress based detachment, Biotechnology and Bioengineering **103**, 92 (2009).

[51] B. E. Rittman, The effect of shear stress on biofilm loss rate, Biotechnology and Bioengineering **24**, 501 (1982).

[52] W. Characklis, M. Trulear, J. Bryers, and N. Zelver, Dynamics of biofilm processes: Methods, Water Research **16**, 1207 (1982).

[53] M. L. Gibiansky, J. C. Conrad, F. Jin, V. D. Gordon, D. A. Motto, M. A. Mathewson, W. G. Stopka, D. C. Zelasko, J. D. Shrout, and G. C. L. Wong, Bacteria use type IV pili to walk upright and detach from surfaces, Science (New York, N.Y.) **330**, 197 (2010).

[54] T. Rossy, C. D. Nadell, and A. Persat, Cellular advective-diffusion drives the emergence of bacterial surface colonization patterns and heterogeneity, Nature Communications **10**, 2471 (2019).

[55] J. Kaplan, Biofilm Dispersal: Mechanisms, Clinical Implications, and Potential Therapeutic Uses, Journal of Dental Research **89**, 205 (2010).

[56] S. C. Chew, S. A. Rice, S. Kjelleberg, and L. Yang, In Situ Mapping of the Mechanical Properties of Biofilms by Particle-tracking Microrheology, Journal of Visualized Experiments : JoVE , 53093 (2015).

[57] T. A. Waigh, Advances in the microrheology of complex fluids, Reports on Progress in Physics. Physical Society (Great Britain) **79**, 074601 (2016).

[58] J. A. McGlynn, N. Wu, and K. M. Schultz, Multiple particle tracking microrheological characterization: Fundamentals, emerging techniques and applications, Journal of Applied Physics **127**, 201101 (2020).

[59] J. W. Hart, T. A. Waigh, J. R. Lu, and I. S. Roberts, Microrheology and Spatial Heterogeneity of Staphylococcus aureus Biofilms Modulated by Hydrodynamic Shear and Biofilm-Degrading Enzymes, Langmuir: the ACS journal of surfaces and colloids **35**, 3553 (2019).

[60] A. Birjiniuk, N. Billings, E. Nance, J. Hanes, K. Ribbeck, and P. S. Doyle, Single particle tracking reveals spatial and dynamic organization of the E. coli biofilm matrix, New Journal of Physics **16**, 085014 (2014).

[61] H. Cao, O. Habimana, A. Safari, R. Heffernan, Y. Dai, and E. Casey, Revealing region-specific biofilm viscoelastic properties by means of a micro-rheological approach, npj Biofilms and Microbiomes **2**, 1 (2016).

[62] M. U. Rahman, D. F. Fleming, I. Sinha, K. P. Rumbaugh, V. D. Gordon, and G. F. Christopher, Effect of collagen and EPS components on the viscoelasticity of *Pseudomonas aeruginosa* biofilms, Soft Matter **17**, 6225 (2021).

[63] S. S. Rogers, C. Van Der Walle, and T. A. Waigh, Microrheology of Bacterial Biofilms In Vitro: *Staphylococcus aureus* and *Pseudomonas aeruginosa*, Langmuir : the ACS journal of surfaces and colloids **24**, 13549 (2008).

[64] P. Stoodley, R. Cargo, C. J. Rupp, S. Wilson, and I. Klapper, Biofilm material properties as related to shear-induced deformation and detachment phenomena, Journal of Industrial Microbiology & Biotechnology **29**, 361 (2002).

[65] I. Klapper, C. J. Rupp, R. Cargo, B. Purvedorj, and P. Stoodley, Viscoelastic fluid description of bacterial biofilm material properties, Biotechnology and Bioengineering **80**, 289 (2002).

[66] T. G. Mason, H. Gang, and D. A. Weitz, Rheology of complex fluids measured by dynamic light scattering, Journal of Molecular Structure Horizons in Small Angle Scattering From Mesoscopic Systems, **383**, 81 (1996).

[67] T. G. Mason, K. Ganesan, J. H. van Zanten, D. Wirtz, and S. C. Kuo, Particle Tracking Microrheology of Complex Fluids, Physical Review Letters **79**, 3282 (1997).

[68] Y. Liu and J.-H. Tay, The essential role of hydrodynamic shear force in the formation of biofilm and granular sludge, Water Research **36**, 1653 (2002).

[69] A. León Ohl, H. Horn, and D. C. Hempel, Behaviour of biofilm systems under varying hydrodynamic conditions, Water Science and Technology: A Journal of the International Association on Water Pollution Research **49**, 345 (2004).

[70] C. S. Laspidou and B. E. Rittmann, Evaluating trends in biofilm density using the UMCCA model, Water Research **38**, 3362 (2004).

[71] D. Celmer, J. Oleszkiewicz, and N. Cicek, Impact of shear force on the biofilm structure and performance of a membrane biofilm reactor for tertiary hydrogen-driven denitrification of municipal wastewater, Water Research **42**, 3057 (2008).

[72] J. Yang, S. Cheng, C. Li, Y. Sun, and H. Huang, Shear Stress Affects Biofilm Structure and Consequently Current Generation of Bioanode in Microbial Electrochemical Systems (MESs), Frontiers in Microbiology **10** (2019).

[73] Y. Zhang, D. M. Silva, P. Young, D. Traini, M. Li, H. X. Ong, and S. Cheng, Understanding the effects of aerodynamic and hydrodynamic shear forces on *Pseudomonas aeruginosa* biofilm growth, Biotechnology and Bioengineering **119**, 1483 (2022).

[74] C. Ryder, M. Byrd, and D. J. Wozniak, Role of polysaccharides in Pseudomonas aeruginosa biofilm development, Current Opinion in Microbiology **10**, 644 (2007).

[75] K. M. Colvin, Y. Irie, C. S. Tart, R. Urbano, J. C. Whitney, C. Ryder, P. L. Howell, D. J. Wozniak, and M. R. Parsek, The Pel and Psl polysaccharides provide Pseudomonas aeruginosa structural redundancy within the biofilm matrix, Environmental microbiology **14**, 10.1111/j.1462 (2012).

[76] K. M. Colvin, V. D. Gordon, K. Murakami, B. R. Borlee, D. J. Wozniak, G. C. L. Wong, and M. R. Parsek, The Pel Polysaccharide Can Serve a Structural and Protective Role in the Biofilm Matrix of Pseudomonas aeruginosa, PLoS Pathogens **7**, e1001264 (2011).

[77] J. M. Ghigo, Natural conjugative plasmids induce bacterial biofilm development, Nature **412**, 442 (2001).

[78] M. Colón-González, M. Méndez-Ortiz, and J. Membrillo-Hernández, Anaerobic growth does not support biofilm formation in Escherichia coli K-12, Research in Microbiology **155**, 514 (2004).

[79] W. Sabra, E.-J. Kim, and A.-P. Zeng, Physiological responses of Pseudomonas aeruginosa PAO1 to oxidative stress in controlled microaerobic and aerobic cultures, Microbiology (Reading, England) **148**, 3195 (2002).

[80] C. Alvarez-Ortega and C. S. Harwood, Responses of Pseudomonas aeruginosa to low oxygen indicate that growth in the cystic fibrosis lung is by aerobic respiration, Molecular microbi-

ology **65**, 153 (2007).

[81] G. Ceriotti, S. M. Borisov, J. S. Berg, and P. de Anna, Morphology and Size of Bacterial Colonies Control Anoxic Microenvironment Formation in Porous Media, Environmental Science & Technology **56**, 17471 (2022).

[82] H.-M. Wu, T.-A. Lee, P.-L. Ko, W.-H. Liao, T.-H. Hsieh, and Y.-C. Tung, Widefield frequency domain fluorescence lifetime imaging microscopy (FD-FLIM) for accurate measurement of oxygen gradients within microfluidic devices, Analyst **144**, 3494 (2019).

[83] P. S. Stewart and M. J. Franklin, Physiological heterogeneity in biofilms, Nature Reviews Microbiology **6**, 199 (2008).

[84] J. Jo, A. Price-Whelan, and L. E. P. Dietrich, Gradients and consequences of heterogeneity in biofilms, Nature reviews. Microbiology **20**, 593 (2022).

[85] T. Rasamiravaka, Q. Labtani, P. Duez, and M. El Jaziri, The Formation of Biofilms by *Pseudomonas aeruginosa* : A Review of the Natural and Synthetic Compounds Interfering with Control Mechanisms, BioMed Research International **2015**, 1 (2015).

[86] A. B. Cunningham, W. G. Characklis, F. Abedeen, and D. Crawford, Influence of biofilm accumulation on porous media hydrodynamics, Environmental Science & Technology **25**, 1305 (1991), publisher: American Chemical Society.

[87] P. Desmond, K. T. Huisman, H. Sanawar, N. M. Farhat, J. Traber, E. O. Fridjonsson, M. L. Johns, H.-C. Flemming, C. Picioreanu, and J. S. Vrouwenvelder, Controlling the hydraulic resistance of membrane biofilms by engineering biofilm physical structure, Water Research **210**, 118031 (2022).

[88] G. Wei and J. Q. Yang, Microfluidic investigation of the impacts of flow fluctuations on the development of Pseudomonas putida biofilms, npj Biofilms and Microbiomes **9**, 73 (2023).

[89] T. L. Stewart and H. Scott Fogler, Pore-scale investigation of biomass plug development and propagation in porous media, Biotechnology and Bioengineering **77**, 577 (2002).

[90] M. R. Nejadnik, H. C. Van Der Mei, H. J. Busscher, and W. Norde, Determination of the Shear Force at the Balance between Bacterial Attachment and Detachment in Weak-Adherence Systems, Using a Flow Displacement Chamber, Applied and Environmental Microbiology **74**, 916 (2008).

[91] T. Saur, E. Morin, F. Habouzit, N. Bernet, and R. Escudié, Impact of wall shear stress on initial bacterial adhesion in rotating annular reactor, PLOS ONE **12**, e0172113 (2017), publisher: Public Library of Science.

[92] A. Park, H.-H. Jeong, J. Lee, K. P. Kim, and C.-S. Lee, Effect of shear stress on the formation of bacterial biofilm in a microfluidic channel, BioChip Journal **5**, 236 (2011).

[93] G. Wei and J. Q. Yang, Impacts of hydrodynamic conditions and microscale surface roughness on the critical shear stress to develop and thickness of early-stage Pseudomonas putida biofilms, Biotechnology and Bioengineering **120**, 1797 (2023), _eprint:

https://onlinelibrary.wiley.com/doi/pdf/10.1002/bit.28409.

[94] J. A. Howell and B. Atkinson, Sloughing of microbial film in trickling filters, Water Research **10**, 307 (1976).

[95] L. Talon, On the determination of a generalized Darcy equation for yield stress fluid in porous media, Science Talks **3**, 100042 (2022).

[96] R. Sharp, P. Stoodley, M. Adgie, R. Gerlach, and A. Cunningham, Visualization and characterization of dynamic patterns of flow, growth and activity of biofilms growing in porous media, Water Science and Technology **52**, 85 (2005).

[97] S. Bottero, T. Storck, T. J. Heimovaara, M. C. Van Loosdrecht, M. V. Enzien, and C. Picioreanu, Biofilm development and the dynamics of preferential flow paths in porous media, Biofouling **29**, 1069 (2013).

[98] M. Wagner, B. Manz, F. Volke, T. R. Neu, and H. Horn, Online assessment of biofilm development, sloughing and forced detachment in tube reactor by means of magnetic resonance microscopy, Biotechnology and Bioengineering **107**, 172 (2010).

[99] E. Paul, J. C. Ochoa, Y. Pechaud, Y. Liu, and A. Liné, Effect of shear stress and growth conditions on detachment and physical properties of biofilms, Water Research **46**, 5499 (2012).

[100] D. J. Stickler, Clinical complications of urinary catheters caused by crystalline biofilms: Something needs to be done, Journal of Internal Medicine **276**, 120 (2014).

[101] E. Guaglianone, R. Cardines, C. Vuotto, R. Di Rosa, V. Babini, P. Mastrantonio, and G. Donelli, Microbial biofilms associated with biliary stent clogging, FEMS Immunology & Medical Microbiology **59**, 410 (2010).

[102] Z. Jiang, T. Nero, S. Mukherjee, R. Olson, and J. Yan, Searching for the Secret of Stickiness: How Biofilms Adhere to Surfaces, Frontiers in Microbiology **12**, 10.3389/fmicb.2021.686793 (2021).

[103] A. Ohashi and H. Harada, A novel concept for evaluation of biofilm adhesion strength by applying tensile force and shear force, Water Science and Technology Water Quality International '96 Part 3: Modelling of Activated Sludge Processes; Microorganisms in Activated Sludge and Biofilm Processes; Anareobic Biological Treatment; Biofouling, **34**, 201 (1996).

[104] M. Chen, Z. Zhang, and T. Bott, Direct measurement of the adhesive strength of biofilms in pipes by micromanipulation, Biotechnology Techniques **12**, 875 (1998).

[105] P. C. Y. Lau, J. R. Dutcher, T. J. Beveridge, and J. S. Lam, Absolute Quantitation of Bacterial Biofilm Adhesion and Viscoelasticity by Microbead Force Spectroscopy, Biophysical Journal **96**, 2935 (2009).

[106] V. Körstgens, H. C. Flemming, J. Wingender, and W. Borchard, Uniaxial compression measurement device for investigation of the mechanical stability of biofilms, Journal of Microbiological Methods **46**, 9 (2001).

[107] S. H. Lee, E. Secchi, and P. K. Kang, Rapid formation of bioaggregates and morphology transition to biofilm streamers induced by pore-throat flows, Proceedings of the National Academy of Sciences **120**, e2204466120 (2023).

[108] C. J. Rupp, C. A. Fux, and P. Stoodley, Viscoelasticity of Staphylococcus aureus Biofilms in Response to Fluid Shear Allows Resistance to Detachment and Facilitates Rolling Migration, Applied and Environmental Microbiology **71**, 2175 (2005).

[109] L. Pavlovsky, J. G. Younger, and M. J. Solomon, In situ rheology of Staphylococcus epidermidis bacterial biofilms, Soft Matter **9**, 122 (2013).

[110] B. O. Emerenini, B. A. Hense, C. Kuttler, and H. J. Eberl, A Mathematical Model of Quorum Sensing Induced Biofilm Detachment, PLOS ONE **10**, e0132385 (21 juil. 2015).

[111] B. R. Boles, M. Thoendel, and P. K. Singh, Rhamnolipids mediate detachment of Pseudomonas aeruginosa from biofilms, Molecular Microbiology **57**, 1210 (2005), _eprint: https://onlinelibrary.wiley.com/doi/pdf/10.1111/j.1365-2958.2005.04743.x.

[112] M. R. Mattei, L. Frunzo, B. D'Acunto, Y. Pechaud, F. Pirozzi, and G. Esposito, Continuum and discrete approach in modeling biofilm development and structure: A review, Journal of Mathematical Biology **76**, 945 (2018).

[113] S. Wilson, M. A. Hamilton, G. C. Hamilton, M. R. Schumann, and P. Stoodley, Statistical Quantification of Detachment Rates and Size Distributions of Cell Clumps from Wild-Type (PAO1) and Cell Signaling Mutant (JP1) *Pseudomonas aeruginosa* Biofilms, Applied and Environmental Microbiology **70**, 5847 (2004).

[114] A. Bohn, B. Zippel, J. S. Almeida, and J. B. Xavier, Stochastic modeling for characterisation of biofilm development with discrete detachment events (sloughing), Water Science and Technology: A Journal of the International Association on Water Pollution Research **55**, 257 (2007).

[115] Z. Lewandowski, H. Beyenal, and D. Stookey, Reproducibility of biofilm processes and the meaning of steady state in biofilm reactors, Water Science and Technology: A Journal of the International Association on Water Pollution Research **49**, 359 (2004).

[116] R. Maaß, M. Wraith, J. T. Uhl, J. R. Greer, and K. A. Dahmen, Slip statistics of dislocation avalanches under different loading modes, Physical Review E **91**, 042403 (2015).

[117] Á. Corral, Long-Term Clustering, Scaling, and Universality in the Temporal Occurrence of Earthquakes, Physical Review Letters **92**, 108501 (2004).

[118] P. Kumar, E. Korkolis, R. Benzi, D. Denisov, A. Niemeijer, P. Schall, F. Toschi, and J. Trampert, On interevent time distributions of avalanche dynamics, Scientific Reports **10**, 626 (2020).

[119] S. Berg, D. Kutra, T. Kroeger, C. N. Straehle, B. X. Kausler, C. Haubold, M. Schiegg, J. Ales, T. Beier, M. Rudy, K. Eren, J. I. Cervantes, B. Xu, F. Beuttenmueller, A. Wolny, C. Zhang, U. Koethe, F. A. Hamprecht, and A. Kreshuk, Ilastik: Interactive machine learning

for (bio)image analysis, Nature Methods **16**, 1226 (2019).

[120] C. A. Schneider, W. S. Rasband, and K. W. Eliceiri, NIH Image to ImageJ: 25 years of Image Analysis, Nature methods **9**, 671 (2012).

[121] C. Torrence and G. P. Compo, A Practical Guide to Wavelet Analysis, Bulletin of the American Meteorological Society **79**, 61 (1998).

[122] P. Welch, The use of fast Fourier transform for the estimation of power spectra: A method based on time averaging over short, modified periodograms, IEEE Transactions on Audio and Electroacoustics **15**, 70 (1967).

[123] B. Maier, How Physical Interactions Shape Bacterial Biofilms, Annual Review of Biophysics **50**, 401 (2021).

[124] T. Maier and T. Haraszti, Python algorithms in particle tracking microrheology, Chemistry Central Journal **6**, 144 (2012).

[125] S. C. Chew, S. A. Rice, S. Kjelleberg, and L. Yang, In Situ Mapping of the Mechanical Properties of Biofilms by Particle-tracking Microrheology, Journal of Visualized Experiments , 53093 (2015).

[126] T. G. Mason, H. Gang, and D. A. Weitz, Rheology of complex fluids measured by dynamic light scattering, Journal of Molecular Structure S0022-2860(96)09272-1 (1996).

[127] J. C. Crocker, M. T. Valentine, E. R. Weeks, T. Gisler, P. D. Kaplan, A. G. Yodh, and D. A. Weitz, Two-Point Microrheology of Inhomogeneous Soft Materials, Physical Review Letters **85**, 888 (2000).